Diffraction anomalous fine structure: Unifying x-ray diffraction and x-ray absorption with DAFS

Larry B. Sorensen, Julie O. Cross, M. Newville, B. Ravel, J.J. Rehr and H. Stragier[a]
C.E. Bouldin and J.C. Woicik[b]

[a]Department of Physics, University of Washington, Seattle, Wa. 98195, U.S.A.

[b]National Institute of Standards and Technology, Gaithersburg, Md. 20899, U.S.A.

Abstract

This chapter describes a developing x-ray spectroscopic, structural, and crystallographic method called the diffraction anomalous fine structure technique (DAFS), which measures the elastic Bragg reflection intensities versus photon energy. This new method combines the long-range order and crystallographic sensitivities of x-ray diffraction with the spectroscopic and short-range order sensitivities of x-ray absorption techniques.

In the extended fine structure region, DAFS provides the same short-range structural information as EXAFS: the bond lengths, coordination numbers, neighbor types, and bond disorders for the atoms surrounding the resonantly scattering atoms. In the near-edge region, DAFS provides the same structural and spectroscopic sensitivities as XANES: the valence, empty orbital and bonding information for the resonant atoms.

Because DAFS combines the capabilities of diffraction, EXAFS and XANES into a single technique, it has two enhanced sensitivities compared to the separate techniques: (1) Wavevector selectivity. DAFS can provide EXAFS- and XANES-like information for the specific subset of atoms selected by the diffraction condition. (2) Site selectivity. DAFS can provide site-specific absorption-like spectroscopic and structural information for the inequivalent sites of a single atomic species within the unit cell.

We present the theory, experimental methods, and analysis techniques that we have developed, and we show that they work very precisely for Cu metal. We also show that DAFS can yield its enhanced sensitivities while maintaining a precision comparable to that of the best EXAFS and XANES measurements. Wavevector selectivity is demonstrated with a study of a buried 400Å thick $In_{0.2}Ga_{0.8}As$ layer which is wavevector separated from its GaAs substrate and cap. Site selectivity is demonstrated with a study of the two inequivalent Cu sites in a 2400Å thick $YBa_2Cu_3O_{6.6}$ superconductor film.

1. INTRODUCTION

The presence of oscillatory fine structure in the x-ray absorption spectra of atoms in solids has been known for over 70 years [1], and the analogous fine structure in x-ray diffraction has been known for almost 40 years [2]. It was not until intense synchrotron radiation sources became available, however, that the extended x-ray absorption fine

structure technique (EXAFS) [3] became a routine spectroscopic method. In the last few years, with the development of modern multiple scattering MS-XAFS theory and analysis techniques, EXAFS has realized its potential as an accurate probe of distances and structure [4]. Recently, again because of synchrotron radiation sources, the diffraction anomalous fine structure technique (DAFS) has started to be used as a combined spectroscopic, structural, and crystallographic method [5–11]. Because the diffraction and absorption fine structures are closely related by unitarity and causality, the same sophisticated MS-XAFS techniques can be applied to DAFS measurements. This chapter describes the theoretical and experimental considerations behind DAFS, explains how DAFS measurements can be analyzed using unitarity and causality to relate and to isolate the real and imaginary components of the scattering amplitude, and illustrates how generalized MS-DAFS theory can be used to analyze the isolated diffraction fine structure.

The common physical origin of DAFS and XAFS is illustrated schematically in Fig. 1. In both DAFS and XAFS, the incoming photon promotes an electron from a compact

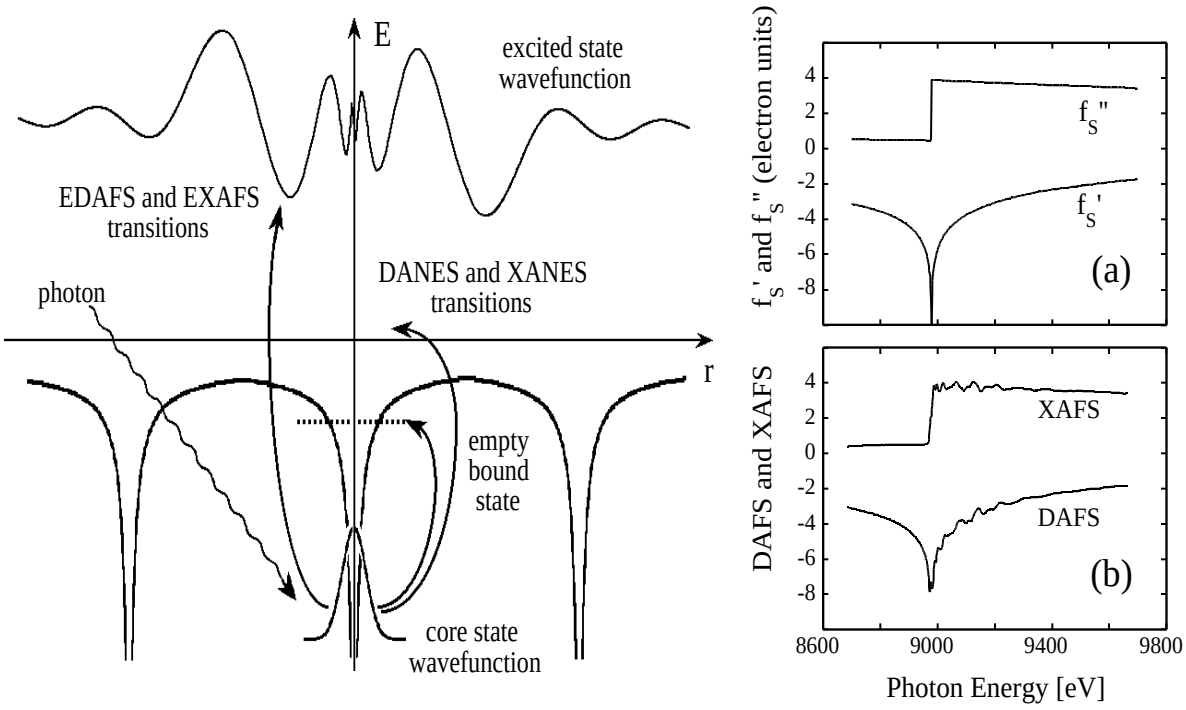

Figure 1. The one-electron picture for the origin of the DAFS and XAFS fine structure. The excited state wavefunction is shown for a 200 eV photoelectron in a fully screened Cu atom without neighbors. When neighbors are present, the wavefunction is changed, and these changes versus photon energy produce the oscillatory DAFS and XAFS signals. (a) The calculated Cromer-Liberman real and imaginary scattering amplitudes for Cu have a smooth cusp in f_s' and a step in f_s''. Throughout this chapter, the steps are shown in their conventional positive form [12]. (b) The measured DAFS and XAFS signals both have extended oscillations versus the photon energy. These extended oscillations provide structural and spectroscopic information about the atoms and their neighbors.

core state to an empty continuum state, or to an empty bound state. When the electron is promoted to the continuum states at least 30 eV above the edge, the absorption and diffraction oscillatory fine structure signals are called EXAFS and EDAFS, respectively [3]. When the electron is promoted to an empty bound state, or to the continuum states below about 30 eV, the fine structure signals are called XANES and DANES [3]. The intensity of the DAFS and XAFS signals for each photon energy depends on the matrix elements between the ground state wavefunction (the core state) and the excited state wavefunction. For the EDAFS and EXAFS signals, the intensities depend on how well the excited state wavefunctions fit into the "effective boxes" produced by the central atom and the neighbors. For a simple box, these interference effects would vary as $\sin(2KR_j + \Phi_j)$, where the photoelectron wavenumber $K = (2m(E - E_0)/\hbar^2)^{\frac{1}{2}}$ depends on the difference between the photon energy, E, and the electron binding energy, E_0. Note that the interference effects depend on the size of the box, which is set by the bond length, R_j, between the central atom and the neighboring atom. Thus in this simple case, the oscillatory fine structure would consist of a sum over all the neighbors, labeled by j, of $\sin(2KR_j + \Phi_j)$ terms. Because the walls of the "real boxes" are formed by the screened excited central atom and by the surrounding atoms, there are photoelectron wavenumber dependent phase shifts, $\Phi_j(K) = \phi_j(K) + 2\delta_c(K)$, that slightly complicate the analysis. Fortunately, the recent theoretical MS-XAFS advances have made it possible to calculate the EDAFS and EXAFS signals precisely, and the full power of these techniques can now be obtained routinely [4].

The physical origin of the causal relationship between the real and imaginary components of the forward scattering amplitude, and the connection between the forward dispersion relations and the analyticity of the scattering amplitude, are discussed very clearly by Toll [13]. Toll uses a proof by contradiction (see Fig. 2): Assume that a system could absorb some frequency components without disturbing any of the other frequency components, and consider the incoming Gaussian packet shown in Fig. 2a, which is composed of many different frequency components which extend over all time. Its central frequency components are shown in Fig. 2b. If the hypothetical system could absorb just these central components, with no change in the remaining components, then the output would be the original packet minus the absorbed components shown in Fig. 2c. This, however, would clearly violate causality because there would be an output before the incoming packet reaches the absorber. Therefore, the system cannot absorb some frequency components without phase shifting the remaining components to maintain zero output before the input arrives. *Absorption and dispersion are intimately connected.* Figure 2d shows the hypothetical output if the central frequency components are phase shifted by the imaginary component of the system's non-forward scattering amplitude, instead of being absorbed. Again this would clearly violate causality. *At a fixed momentum transfer, the real and the imaginary components of the scattering amplitude are intimately connected.* For each incoming and outgoing direction, the complex scattering amplitude is an analytic function of the energy. Consequently, the real and imaginary components of the scattering amplitude are related by Cauchy's theorem: they are a Kramers-Kronig or Hilbert transform pair.

The argument given above explains why the real and imaginary components of the scattering amplitude in any fixed direction are so closely related. To establish the con-

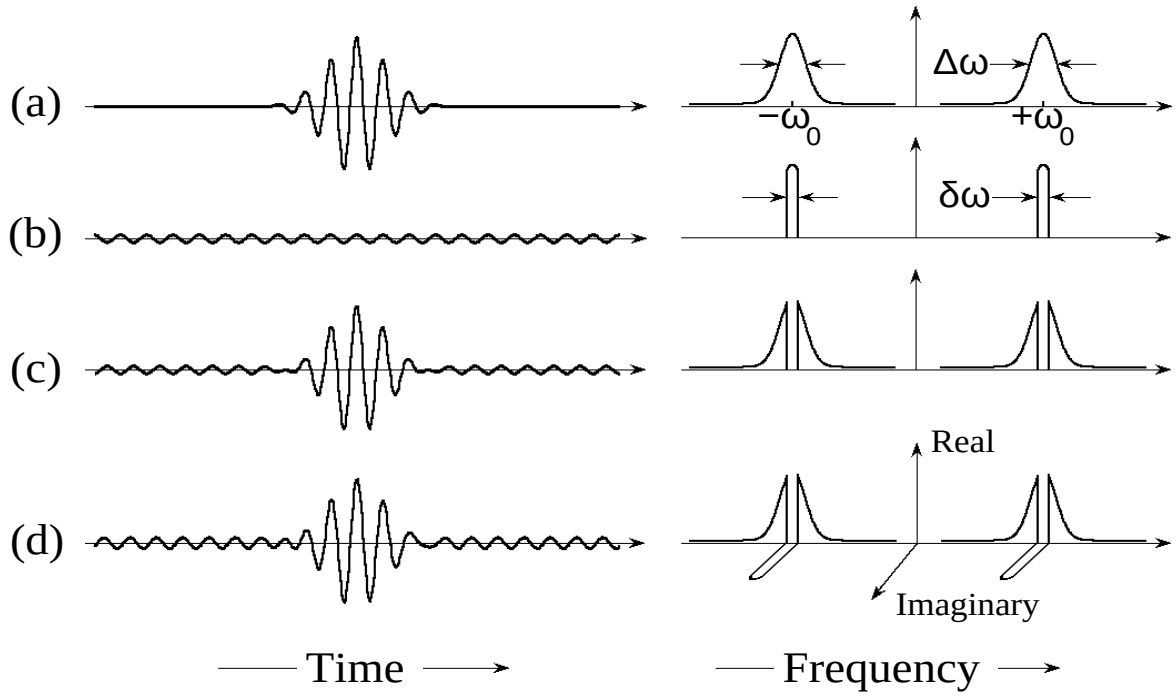

Figure 2. The acausal behavior that would be produced if a system could selectively absorb, or could selectively phase shift, some of the frequency components of a Gaussian wave packet without affecting any of the other frequency components. Both the time and frequency domain signals are shown for: (a) The incident Gaussian packet with $\Delta\omega/\omega_0 = 0.1$. (b) The central frequency components with $\delta\omega/\omega_0 = 5 \times 10^{-3}$, which are to be selectively absorbed or phase shifted. For visual clarity, $\delta\omega$ is shown larger than its actual size in the frequency domain; all of the time domain signals are shown without distortion. (c) The acausal behavior that would be produced by absorbing only the central frequency components. (d) The acausal behavior that would be produced by phase shifting only the central frequency components.

nection between DAFS and XAFS, however, we need a relationship between the forward and non-forward amplitudes. The necessary connection comes from unitarity: To conserve probability, the incoming packet must be either transmitted, absorbed, scattered with a phase shift, or scattered without a phase shift. The optical theorem (a special case of unitarity) tells us that the sum of all the outgoing and absorbed waves must equal the incoming wave. For each photon energy, the optical theorem connects the angular integral of the elastic scattering (DAFS) over all directions to the absorption (XAFS). In general, this is the only connection. In the special case of pure dipole scattering, the scattering amplitude has the same energy dependence in all directions. Consequently, for pure dipole scattering the energy dependence of the imaginary component of the scattering amplitude is identical to that of the absorption, and the energy dependence of the real component is given by the Kramers-Kronig transform of the absorption. Because x-ray scattering is often predominantly dipolar, DAFS and XAFS can usually be related by angle independent Kramers-Kronig transforms.

2. DAFS THEORY

This section describes the resonant and non-resonant atomic scattering amplitudes, and shows how the atomic components combine to produce the observed smooth and oscillatory DAFS and XAFS signals from a crystal.

2.1. Form of the Thomson and anomalous amplitudes

In non-relativistic quantum mechanics, neglecting the magnetic scattering terms, the total atomic scattering amplitude, $f = f_0 + \Delta f$, for photons with energy $E = \hbar\omega$ and with incident and scattered momenta $\mathbf{k}_1$ and $\mathbf{k}_2$, is the sum of the non-resonant Thomson scattering amplitude, f_0, and the "anomalous" scattering amplitude, Δf (see Fig. 3).

The Thompson and anomalous scattering amplitudes are given, in terms of the classical single electron scattering amplitude, $r_0 = e^2/mc^2$, by [12, 14–16]

$$f_0(\mathbf{k}_2 - \mathbf{k}_1) = f_0(\mathbf{Q}) = -r_0\ \hat{\mathbf{e}}_2^*\cdot\hat{\mathbf{e}}_1 \sum_j\ \langle j|e^{-i(\mathbf{k}_2-\mathbf{k}_1)\cdot\mathbf{r}}|j\rangle, \tag{1}$$

$$\begin{aligned}\Delta f(\mathbf{k}_1,\mathbf{k}_2,E) &= f'(\mathbf{k}_1,\mathbf{k}_2,E) + if''(\mathbf{k}_1,\mathbf{k}_2,E) \\ &= \frac{r_0}{m}\ \sum_j\sum_n\ \frac{\langle j|\hat{\mathbf{e}}_2^*\cdot\mathbf{p}e^{-i\mathbf{k}_2\cdot\mathbf{r}}|n\rangle\langle n|\hat{\mathbf{e}}_1\cdot\mathbf{p}e^{+i\mathbf{k}_1\cdot\mathbf{r}}|j\rangle}{E_n - E_j - \hbar\omega + (\Delta_n - \frac{1}{2}i\Gamma_n)} \\ &\qquad + \frac{\langle j|\hat{\mathbf{e}}_1\cdot\mathbf{p}e^{+i\mathbf{k}_1\cdot\mathbf{r}}|n\rangle\langle n|\hat{\mathbf{e}}_2^*\cdot\mathbf{p}e^{-i\mathbf{k}_2\cdot\mathbf{r}}|j\rangle}{E_n - E_j + \hbar\omega}.\end{aligned} \tag{2}$$

The self-energy corrections that produce the Lamb-shift $\Delta_n(E_n+\hbar\omega)$ and the linewidth $\Gamma_n(E_n+\hbar\omega)$ of the resonant term are shown explicitly [15].

The Thomson amplitude is a scalar which depends on the photon momentum transfer, $\hbar\mathbf{Q} = \hbar(\mathbf{k}_2 - \mathbf{k}_1)$, and on the photon polarization factors, $\hat{\mathbf{e}}_2^*\cdot\hat{\mathbf{e}}_1$, but is independent of the photon energy. The Thomson amplitude is proportional to the Fourier transform of the atom's electronic charge distribution. In contrast, the anomalous amplitude depends separately on the incident and scattered wavevectors, $\mathbf{k}_1$ and $\mathbf{k}_2$, and also depends on the photon energy, E. Thus, in general, Δf is a tensor which depends on the matrix elements between the ground state and the virtual intermediate states, and is not proportional to the Fourier transform of the total or subshell charge density [17]. It has been established experimentally, however, that the $\mathbf{k}_1$ and $\mathbf{k}_2$ dependencies of anomalous scattering are often small, and the full photon energy- and momenta-dependent $\Delta f(\mathbf{k}_1,\mathbf{k}_2,E)$ is conventionally [14] approximated by its momenta-independent forward scattering limit, denoted $\Delta f(E) = f'(E) + if''(E)$. Consequently, the total atomic scattering amplitude, f, depends on the photon energy, E, via its f' and f'' terms, and on the wavevector transfer, $\mathbf{Q}$, via its f_0 term.

2.2. Separation of the smooth and oscillatory DAFS terms

For an atom in a solid, the total atomic scattering amplitude can be subdivided into smooth and oscillating fine structure components,

$$f(\mathbf{Q},E) = [f_0(\mathbf{Q}) + f_s'(E) + if_s''(E)]\ +\ [f_s''(E)\tilde{\chi}(E)]. \tag{3}$$

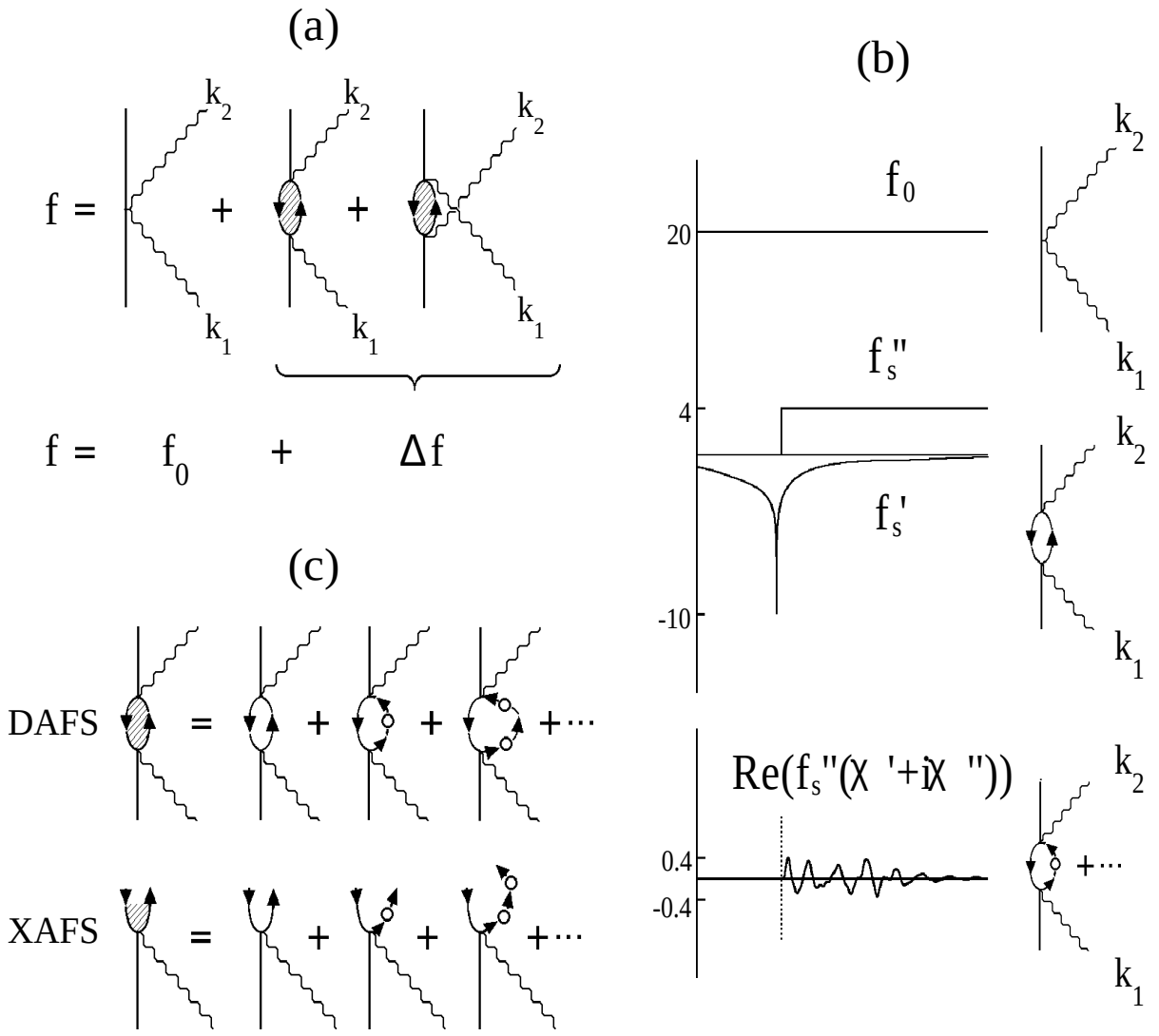

Figure 3. (a) The total nonrelativistic photon-atom scattering amplitude, f, is the sum of three contributions: the non-resonant Thomson amplitude, f_0, and the resonant and antiresonant amplitudes that together are called the "anomalous" amplitude, Δf, which can be divided into smooth and oscillatory components: $\Delta f = [f_s' + i f_s''] + [f_s''(\chi' + i\chi'')]$. (b) The relative sizes of the contributions due to f_0, f_s', f_s'' and $f_s''(\chi' + \chi'')$ are shown for Cu in electron units [12]. (c) The DAFS and XAFS signals are generated by the quantum mechanical interference of the photoelectrons moving through the atoms. In XAFS there is a real photoelectron in the final state, and the interference can be calculated as a sum over photoelectron reflections from the neighbors. In DAFS there is a virtual photoelectron in the transient intermediate state, and the interference can be calculated as a sum over virtual photoelectron reflections from the neighbors. To calculate the DAFS and XAFS signals, we must sum over all possible photoelectron paths. The sum over paths without reflections from the neighbors produces the smooth $f_s' + i f_s''$ component. The sum over paths with reflections produces the oscillatory $f_s''(\chi' + i\chi'')$ component.

The smooth component is given by $f_0(\mathbf{Q}) + f_s'(E) + if_s''(E)$, and its smooth anomalous term, $f_s'(E)+if_s''(E)$, is usually calculated using the Cromer and Liberman method [18]. The correct values of $f_s'(E)+if_s''(E)$, however, are given by embedded atom anomalous amplitudes [19]. For the systems discussed in this chapter, the embedded atom corrections were small, and consequently Cromer-Liberman values were used. When there are neighboring atoms, the oscillating component, $f_s''(E)\tilde{\chi}(E)$, with the DAFS complex-valued $\tilde{\chi} = \chi' + i\chi''$, contains the spectroscopic and structural information. This separation of f into smooth and oscillatory DAFS components is analogous to the usual XAFS separation of μ into smooth μ_0 and oscillatory χ_μ terms: $\mu(E) = \mu_0(E) + \mu_0(E)\chi_\mu(E)$.

2.3. Calculation of the EDAFS contributions using FEFF

As discussed in the introduction, DAFS is intimately connected to XAFS by unitarity and causality. Here, we describe the calculation of the diffraction fine structure using the causal, unitary generalization of the MS-XAFS formalism. The original EXAFS theories were single-scattering plane-wave theories [20]. The curved-wave and multiple-scattering effects can be quite important, however, and recently an accurate and computationally efficient code, called FEFF, which includes these effects, has been developed [4].

FEFF calculates the full complex-valued fine structure function $\tilde{\chi}$ by summing over all possible photoelectron scattering paths,

$$\tilde{\chi}(K) = \sum_{j=1}^{N} \frac{S_0^2}{KR_j^2} \, |f_j(K)| \, \exp[i(2KR_j + \phi_j(K) + 2\delta_c(K))] \, e^{-2\sigma_j^2 K^2} e^{-2R_j/\Lambda(K)}, \tag{4}$$

where the photoelectron wavenumber, K, is related to the incident photon energy E and the binding energy E_0 by $K = (2m(E-E_0)/\hbar^2)^{\frac{1}{2}}$; j is the index of a particular scattering path; N is the total number of possible paths; S_0^2 is the many-body amplitude reduction factor; R_j is the effective path length of path j (which is 1/2 of the total path length); $f_j = |f_j| \exp(i\phi_j(K))$ is the effective curved wave scattering amplitude for path j; $\delta_c(K)$ is the $l = 1$ phase shift at the atom which emits the photoelectron; σ_j^2 is the effective XAFS Debye-Waller factor for the path; and $\Lambda(K)$ is the combined mean free path and core hole lifetime factor.

All state-of-the-art theoretical EXAFS codes actually calculate the full complex-valued x-ray diffraction $\tilde{\chi}(K)$ and use the imaginary part to obtain the XAFS χ_μ,

$$\chi_\mu(K) = \sum_{j=1}^{N} \frac{S_0^2}{KR_j^2} \, |f_j(K)| \, \sin(2KR_j + \phi_j(K) + 2\delta_c(K)) \, e^{-2\sigma_j^2 K^2} e^{-2R_j/\Lambda(K)}. \tag{5}$$

2.4. The DAFS kinematic unit cell structure factor

In the kinematic scattering limit, the measured DAFS intensity is proportional to the square of the unit cell structure factor, $F(\mathbf{Q}, E)$, times an x-ray absorption correction factor, $A(\mathbf{Q}, E)$,

$$I_M(\mathbf{Q}, E) \sim |F(\mathbf{Q}, E)|^2 \, A(\mathbf{Q}, E). \tag{6}$$

The x-ray absorption correction factor for a symmetric Bragg reflection from a sample of thickness t is given by $A(\mathbf{Q}, E) = [1 - \exp(-2\mu t/\sin\theta)]/2\mu$. Note that absorption produces additional fine structure in the measured DAFS intensities due to the XAFS modulation of the x-ray absorption coefficient, $\mu(E) = \mu_0(E)(1 + \chi_\mu(E))$.

There are both real and imaginary x-ray scattering contributions to the DAFS oscillations which come from the individual atomic $(\chi' + i\chi'')_j$ contributions to the unit cell structure factor,

$$F(\mathbf{Q}, E) = \sum_j \left[(f_0 + f_s' + f_s''\chi')_j + i(f_s'' + f_s''\chi'')_j \right] e^{i\mathbf{Q}\cdot\mathbf{r}_j}. \tag{7}$$

To keep the notation compact, we include the anisotropic diffraction Debye-Waller factors implicitly in our $(\quad)_j$ notation: for example,

$$(f_0 + f_s' + if_s'')_j \equiv (f_{0j} + f_{sj}' + if_{sj}'')e^{-<(\mathbf{Q}\cdot\mathbf{u}_j)^2>}. \tag{8}$$

2.5. The DAFS crystallographic weights

To see how DAFS weights different crystallographically inequivalent sites, it is helpful to separate the smooth atomic amplitudes for *all* the atoms in the unit cell, labelled by n, from the fine structure terms for just the resonantly scattering atoms, labelled by l, yielding

$$\begin{aligned} F(\mathbf{Q}, E) &= \sum_n (f_0 + f_s' + if_s'')_n e^{i\mathbf{Q}\cdot\mathbf{r}_n} + \sum_l (f_s''\tilde{\chi})_l e^{i\mathbf{Q}\cdot\mathbf{r}_l} \\ &= A_0 + \sum_l (f_s''\chi' + if_s''\chi'')_l e^{i\mathbf{Q}\cdot\mathbf{r}_l}. \end{aligned} \tag{9}$$

The kinematic diffraction intensity is proportional to the square of the structure factor,

$$\begin{aligned} I(\mathbf{Q}, E) \sim |F|^2 = |A_0|^2 &+ 2\ \mathrm{Re}(A_0) \sum_l \left[(f_s''\chi')_l \cos(\mathbf{Q}\cdot\mathbf{r}_l) - (f_s''\chi'')_l \sin(\mathbf{Q}\cdot\mathbf{r}_l) \right] \\ &+ 2\ \mathrm{Im}(A_0) \sum_l \left[(f_s''\chi')_l \sin(\mathbf{Q}\cdot\mathbf{r}_l) + (f_s''\chi'')_l \cos(\mathbf{Q}\cdot\mathbf{r}_l) \right] \\ &+ |\sum_l (f_s''\chi' + if_s''\chi'')_l e^{i\mathbf{Q}\cdot\mathbf{r}_l}|^2. \end{aligned} \tag{10}$$

The first term, $|A_0|^2$, represents the smooth atomic contributions to the energy dependence of the Bragg intensities. The second and third terms are the cross terms between A_0 and $f_s''(\chi' + i\chi'')$. The fourth term is the second order fine structure contribution and is a smooth function versus photon energy.

Because the leading order DAFS contributions to the intensity come from the cross terms between A_0 and $f_s''\tilde{\chi}$, the leading order site-specific χ_l' and χ_l'' information appears linearly in the Bragg intensities, and can be extracted using standard crystallographic techniques. We can rewrite Eqn. 10 in terms of the crystallographic weights α_m,

$$\begin{aligned} I \sim |A_0|^2 &+ 2\ \mathrm{Re}(A_0) \sum_m (f_s'')_m \left[\chi_m' \mathrm{Re}(\alpha_m) - \chi_m'' \mathrm{Im}(\alpha_m) \right] \\ &+ 2\ \mathrm{Im}(A_0) \sum_m (f_s'')_m \left[\chi_m' \mathrm{Im}(\alpha_m) + \chi_m'' \mathrm{Re}(\alpha_m) \right] + \ \ldots \end{aligned} \tag{11}$$

The site specific crystallographic weights depend on the diffraction wavevector transfer $\mathbf{Q}$ and are given by the sum over all the occurrences in the unit cell of each equivalent site, labelled by k, producing one weight for each inequivalent site, labelled by m,

$$\alpha_m(\mathbf{Q}) = \sum_{\mathbf{r}_k \in \{m\ sites\}} e^{i\mathbf{Q}\cdot\mathbf{r}_k}. \tag{12}$$

2.6. The polarization dependence of the DAFS signals

The tensor properties of Δf are reflected in the polarization dependence of the DAFS signals. The EDAFS polarization dependence is analogous to that of EXAFS. For single-scattering EXAFS, the polarization dependence is $(\hat{\mathbf{e}}\cdot\hat{\mathbf{z}})^2$, where $\hat{\mathbf{z}}$ specifies the direction from the absorbing atom to the back-scattering neighbor; the analogous dependence for EDAFS is $(\hat{\mathbf{e}}_1\cdot\hat{\mathbf{z}})(\hat{\mathbf{e}}_2\cdot\hat{\mathbf{z}})$. For multi-leg single-scattering paths, the EXAFS polarization dependence only depends on the two legs closest to the absorbing atom and is given by $(\hat{\mathbf{e}}\cdot\hat{\mathbf{z}}_1)(\hat{\mathbf{e}}\cdot\hat{\mathbf{z}}_n)$, where $\hat{\mathbf{z}}_1$ and $\hat{\mathbf{z}}_n$ specify the directions of the two closest legs; the analogous dependence for (nonmagnetic) EDAFS is given by $(\hat{\mathbf{e}}_1\cdot\hat{\mathbf{z}}_1)(\hat{\mathbf{e}}_2\cdot\hat{\mathbf{z}}_2)+(\hat{\mathbf{e}}_1\cdot\hat{\mathbf{z}}_2)(\hat{\mathbf{e}}_2\cdot\hat{\mathbf{z}}_1)$.

The DANES and XANES polarization dependences are more complicated. The newest FEFF codes calculate the correct polarization dependence of the XANES matrix elements starting a little above threshold, and over the entire EXAFS region. These full FEFF calculations show that the simple polarization dependence $(\hat{\mathbf{e}}\cdot\hat{\mathbf{z}}_1)(\hat{\mathbf{e}}\cdot\hat{\mathbf{z}}_n)$ works very well in the EXAFS region. The full polarization dependent FEFF codes for DANES and EDAFS are currently under development.

3. EXPERIMENTAL METHODS

The DAFS experiments described in this chapter were performed at the National Synchrotron Light Source (NSLS), using beamline X23A2. The synchrotron radiation source provided an intense continuous energy spectrum, strong collimation, small source size, and a high degree of polarization. An XAFS beamline was chosen because rapid and precise energy scanning is essential for DAFS measurements. The beamline was adapted by adding a 2-circle spectrometer to give it diffraction capabilities. The 2-circle spectrometer had limited reciprocal space coverage, but it was sufficient for all the experiments described in this chapter. All of the work reported here was done using specular Bragg reflections. The configuration of the X23A2 beamline during the DAFS experiments is shown in Fig. 4. In the fixed exit monochromator, Si(220) crystals were

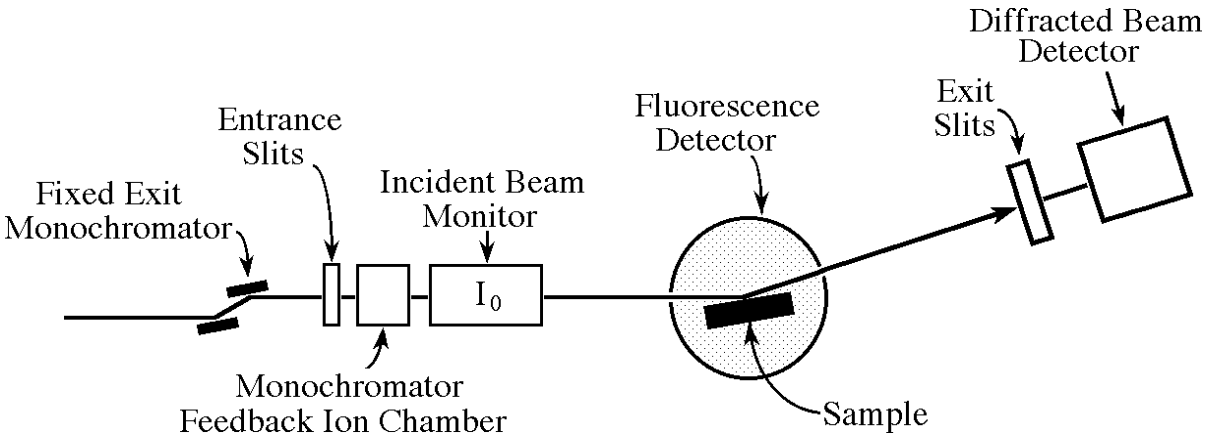

Figure 4. Schematic illustration of the DAFS spectrometer with simultaneous fluorescence XAFS collection.

used for the Cu measurements and Si(311) crystals were used for the $In_{0.2}Ga_{0.8}As$ and $YBa_2Cu_3O_{6.6}$ measurements. The energy calibration procedure is described in reference [21]. During the DAFS experiments, the beamline produced a measured flux of about 5×10^9 photons per second in a 1 mm high by 5 mm wide beam, with a measured energy spread of about 2 eV.

The Bragg diffracted radiation was selected with a 3 mm high by 5 mm wide slit located 27 cm from the sample. This provided adequate suppression of the fluorescence from the sample while accepting essentially all of the diffracted beam. At each energy, the diffractometer was adjusted to keep the momentum transfer fixed; to obtain reliable intensity measurements we found it essential to accurately track the Bragg peak versus energy. For the thin epitaxial film samples we studied, which had broad and smooth mosaic distributions, the peak intensities were proportional to the integrated intensities, and we report here our peak intensity measurements.

We used integral (current mode) techniques to maximize the number of detected photons. Because commercial NaI(Tl) scintillation detectors can only count up to about 2×10^5 photons per second and the samples in this study often had diffracted intensities greater than 10^6 photons per second, both the incident and diffracted x-ray intensities were measured using ionization chambers. The noise, set by photon counting statistics, is proportional to the square-root of the number of detected photons and should be less than the fine structure signal. Since the fine structure signal can be as low as 10^{-4}, at least 10^8 detected photons are required just to reduce the noise to the level of weak fine structure signals. To reduce the sensitivity of the signal and monitor ionization chambers to the second or third harmonics of the 9 Kev fundamental, the gas in each ion chamber was chosen to produce an absorption of about 50% at 9 Kev.

To compensate for the incident intensity variations, we divided the diffracted intensity at each energy by the incident beam monitor signal. The fluorescence from the sample was measured simultaneously with the DAFS signal using a 10 cm diameter ionization chamber [22]. This measured fluorescence signal was used as an energy reference and to allow comparisons of the XAFS and DAFS signals. The measured fluorescence was also used to calculate the absorption corrections for the Cu metal and $YBa_2Cu_3O_{6.6}$ samples.

3.1. Optimization of DAFS measurements

The optimization of a DAFS experiment requires choosing Bragg reflections that balance three factors: intensity, contrast and size of the absorption correction. High intensity reflections are preferred over low intensity reflections for several reasons. Low intensity reflections have poor counting statistics, require long measurement times, and have large background signals due to fluorescence and diffuse scattering. High intensity reflections, however, have poor contrast. The DAFS contrast is a measure of the size of the fine-structure signal relative to the Bragg reflection intensity. Equation 10 shows the intensity dependence on the smooth (A_0) and fine structure (FS) terms,

$$\text{Intensity} \sim |A_0 + FS|^2 \sim |A_0|^2 + 2\text{Re}(A_0)\text{Re}(FS) + 2\text{Im}(A_0)\text{Im}(FS) + |FS|^2. \qquad (13)$$

Because the $|FS|^2$ term is small and smooth, the contrast is roughly proportional to the ratio of the cross terms to $|A_0|^2$.

High intensity Bragg reflections have larger absorption corrections than weak reflections. This is because the absorption contributions are weighted by the $|A_0|^2$ term,

whereas the fine structure contributions from the χ' and χ'' diffraction terms are weighted by $\mathrm{Re}(A_0)$ and $\mathrm{Im}(A_0)$.

All of the samples used for the work described in this chapter were thin epitaxial films grown on substrates. Thin films have several advantages over other samples: they provide more intense diffracted beams than powder samples of the same volume; they typically have broad smooth mosaic distributions which allow easy tracking of the Bragg peaks versus photon energy; their diffracted intensities can be analyzed using the kinematic formalism; and their absorption corrections are relatively small so that optimization consists primarily of finding a compromise between high intensity and high contrast.

There are additional optimization considerations for experiments that use the wavevector and site selectivities of DAFS. For wavevector selective DAFS experiments, Bragg reflections from the desired components should be well separated from the other Bragg reflections. For site selective experiments, Bragg reflections should be chosen that produce easily separable linear combinations of signals from the different sites. Generally, even after applying these restrictions, many suitable Bragg reflections will be available.

4. DAFS ANALYSIS METHODS

For the work described in this chapter, systems with well known structures were chosen so we could demonstrate the enhanced sensitivities of DAFS. The goals of the DAFS analysis were to isolate the fine structure oscillations and, from them, to obtain the detailed wavevector and site selected XAFS-like short-range order information and XANES-like structural, valence and empty orbital information. This section describes the methods that we have developed to isolate the DAFS signals and to analyze the isolated signals. The main steps are listed schematically:

1. Measure the Bragg intensities versus photon energy and apply the standard absorption and diffraction corrections.
   (a) Measure and subtract the background.
   (b) Apply the area, Lorentz-polarization, instrument and absorption corrections.
   (c) Remove any Bragg glitches from the XAFS and determine E_0.
2. Isolate the fine structure using method 2a or 2b.
   (a) Isolate the effective fine structure term χ_e directly from the diffracted intensity using spline methods analogous to conventional XAFS analysis.
   (b) Impose the Kramers-Kronig relation between the real and imaginary components of the DAFS signal, and use an iterative method to extract the real and imaginary components, $f'(E)$ and $f''(E)$, from the data.
3. Use FEFF to analyze the isolated fine structure signals.

The following subsections describe some of the important aspects of these analysis methods. The detailed analysis procedures are described in reference [11].

4.1. Absorption corrections

One of the important corrections is for the absorption of the incident and diffracted x-ray beams as they travel through the sample. Three possible absorption correction methods are:

1. For small absorption corrections, the effective χ_e produced by the direct spline analysis method can be appropriately phase shifted. This method is illustrated by the direct spline analysis of the Cu data presented in Section 5.

2. The absorption correction can be reconstructed from the simultaneous fluorescence measurements. This method is illustrated by the iterative Kramers-Kronig analysis of the Cu and $YBa_2Cu_3O_{6.6}$ data presented in Sections 5, 7 and 8.

3. The absorption correction could also be constructed self-consistently using the f'' functions obtained during the iterative Kramers-Kronig analysis of the DAFS signal.

It is important to remember that the absorption χ_μ signal is different than the DAFS χ' and χ'' signals because XAFS weights the sites based on the number of atoms within the unit cell, whereas DAFS weights the sites crystallographically. Thus measurements of the single χ_μ function are not sufficient to determine the multiple χ' and χ'' functions for systems which contain multiple inequivalent sites.

4.2. Two methods of isolating the diffraction fine structure

The isolation of the diffraction fine structure requires care compared to x-ray absorption analysis because the diffracted intensity is the square of the unit cell structure factor and involves both $f'(E)$ and $f''(E)$. Two useful methods to isolate the fine structure are described in the next subsections.

4.2.1. The direct spline method

The direct spline method is analogous to standard XAFS analysis. It splines the measured DAFS intensity, subtracts the spline from the data, and normalizes the resulting fine structure signal to the spline. In its simplest form, it produces an effective χ_e function that contains a mixture of the χ', χ'' and χ_μ components. If the data is divided by the measured absorption correction before it is splined, the χ_e function will still contain a mixture of χ' and χ'' components. The measured intensity can be related to the theoretical intensity (Eqn. 10) by $I_M = C(E)I$, where $C(E)$ accounts for the energy dependent instrument correction factors. The measured intensity is fit with a smooth spline $S(E) = C(E)|A_0|^2$, and the fine structure is separated from the measured intensity by subtracting the spline from the data. The fine structure is normalized by dividing by $C(E) = S(E)/|A_0|^2$ to yield the effective χ_e function,

$$\begin{aligned}\chi_e(E) &= [I_M - S(E)]|A_0|^2/S(E) \\ &= 2\ \mathrm{Re}(A_0) \sum_m (f_s'')_m\ [\chi'_m \mathrm{Re}(\alpha_m) - \chi''_m \mathrm{Im}(\alpha_m)] \\ &\quad +2\ \mathrm{Im}(A_0) \sum_m (f_s'')_m\ [\chi'_m \mathrm{Im}(\alpha_m) + \chi''_m \mathrm{Re}(\alpha_m)]\,.\end{aligned} \tag{14}$$

Note that the site specific χ'_m and χ''_m signals can be determined from the effective χ_e function if the real and imaginary parts of the smoothly varying background, $\mathrm{Re}(A_0)$ and $\mathrm{Im}(A_0)$, and the crystallographic weights, α_m, can be determined.

4.2.2. The iterative Kramers-Kronig method

The Kramers-Kronig method finds a pair of $f'(E)$ and $f''(E)$ functions which are a self-consistent Kramers-Kronig transform pair, and which also agree with the data. For centrosymmetric systems with crystallographic weights, α_m, this method uses the intensity fitting function,

$$I_{fit} = A(\mathbf{Q}, E)\ N(E) \left[1 + \gamma^2 + 2\beta f' + 2\gamma\beta f'' + \beta^2 \left[(f')^2 + (f'')^2\right]\right], \tag{15}$$

where $\beta = \sum_m \alpha_m / \mathrm{Re}(A_0)$ and $\gamma = \mathrm{Im}(A_0)/\mathrm{Re}(A_0)$, and where the energy dependent instrument correction function $N(E) = m[(E - E_0) + b]$.

To obtain starting values for β, γ, b, and m, f' and f'' are estimated using Cromer-Liberman f'_s and f''_s values, and Eqn. 15 is fit to the data. Then the functions f' and f'' are obtained by using an iterative procedure: Equating the fitting function to the data, the resulting quadratic equation is solved for f'. This f' is then Kramers-Kronig transformed to obtain a corresponding f''. With these new values for f' and f'', the data is refit to obtain new values of β, γ, *etc.*, and in turn a new value for f'. This process usually converges after three or four iterations.

The iterative Kramers-Kronig method has several advantages. First, little knowledge of the crystal structure is required to obtain the f' and f'' functions. Second, the iterative method properly accounts for the diffracted intensity's dependence on the real and imaginary parts of the anomalous amplitude, and also properly accounts for its dependence on the square of the fine structure. Note that the direct method for isolating the fine structure, presented in the previous subsection, neglected the square of the fine structure.

4.3. FEFF analysis of the isolated EDAFS oscillations

Once the fine structure has been isolated and normalized with one of the methods described above, it can be analyzed to obtain local structural information. The analysis proceeds in a manner that is almost identical to modern MS-XAFS analysis : A model of the structure is constructed, and FEFF is used to calculate the amplitude, phase and degeneracy of each photoelectron scattering path. The model is fit to the DAFS data to obtain the desired XAFS-like structural and spectroscopic information [4, 23].

4.4. Information content of DAFS compared to XAFS

Because the DAFS and XAFS signals have limited photoelectron wavenumber "bandwidths", their information content is limited. The number of independent XAFS points is given by $N = 2\Delta R \Delta K/\pi$, where ΔR is the filtering window width in R-space and ΔK is the window width in K-space [24]. For typical values, $\Delta R = 1.5$Å and $\Delta K = 10$Å^{-1}, the number of independent points is approximately 10. This is the maximum number of parameters that can be determined from single shell XAFS data. Note, however, that if there are m inequivalent sites, a set of DAFS measurements for m or more inequivalent reflections can provide up to m times as much information as XAFS. If there are also p

components in the sample, and each component has m inequivalent sites, then a total of (pmN) parameters can be determined per shell.

5. COMPARISON OF DAFS AND XAFS FOR Cu METAL

This section presents a detailed comparison between DAFS and XAFS measurements for Cu metal, which is an ideal system to demonstrate the equivalence of DAFS and XAFS measurements. Cu is a typical XAFS standard and was one of the first systems to be studied by XAFS. It is also an important standard for testing modern XAFS calculations. Cu has a large fine structure, a convenient K-edge energy, and a simple monoatomic FCC lattice. Because of the high symmetry of the Cu lattice, no DAFS polarization corrections are required. The results for the Cu(111) and Cu(222) Bragg reflections presented in this section demonstrate that DAFS measurements contain the same local atomic structural information as XAFS measurements, and confirm in detail the DAFS theory developed in Section 2. Both of the analysis methods described in Section 4 were used with excellent results.

5.1. Cu measurements

The sample was a 25 mm diameter 2000Å thick Cu(111) film grown epitaxially by vapor deposition onto freshly cleaved mica. The c-axis mosaic spread of the film was about 0.25° FWHM, making it relatively easy to track the Bragg peak versus energy. A thin sample was chosen to minimize the effects of sample x-ray absorption. The diffracted intensities at 8500 eV, about 500 eV below the edge, were 3×10^7 photons per second for the Cu(111) Bragg reflection and 1×10^7 photons per second for the Cu(222) reflection. Relative to the incident intensity, the diffracted intensities were 0.6% and 0.2% for these two Bragg reflections, and the diffracted intensities were well described by the kinematic approximation.

The measured intensities versus energy for the Cu(111) and Cu(222) Bragg reflections are shown in Fig. 5a together with the corresponding fluorescence XAFS signal for comparison. The cusp in the Bragg intensity drops at the edge energy, $E_0 = 8978.6$ eV, to about 50% of the pre-edge intensity at 8500 eV for the Cu(111) reflection and to about 25% for the Cu(222) reflection. This difference in the relative cusp drop between the two reflections is caused by the decrease in f_0 with $\mathbf{Q}$. The fine structure oscillations above the absorption edge are present in both the DAFS and XAFS signals and have similar sizes, 12% peak-to-peak, when normalized to their corresponding cusp drop or edge step sizes.

5.2. Direct spline analysis for Cu

Figure 5b shows the diffraction and absorption fine structure signals extracted by the direct spline method from the data in Fig. 5a. The strong similarity between the Cu(111) and the Cu(222) DAFS signals is evident, as is an apparent difference between the two DAFS signals and the XAFS signal. Figure 5c shows the Fourier transform magnitudes of the three signals in Fig. 5b. The agreement between the two DAFS and the XAFS Fourier transforms is very good. Consequently, although the multishell DAFS and XAFS signals in Fig. 5b appear to be different, they actually have identical Fourier magnitudes and therefore can only differ in their phases. Figure 5d shows that,

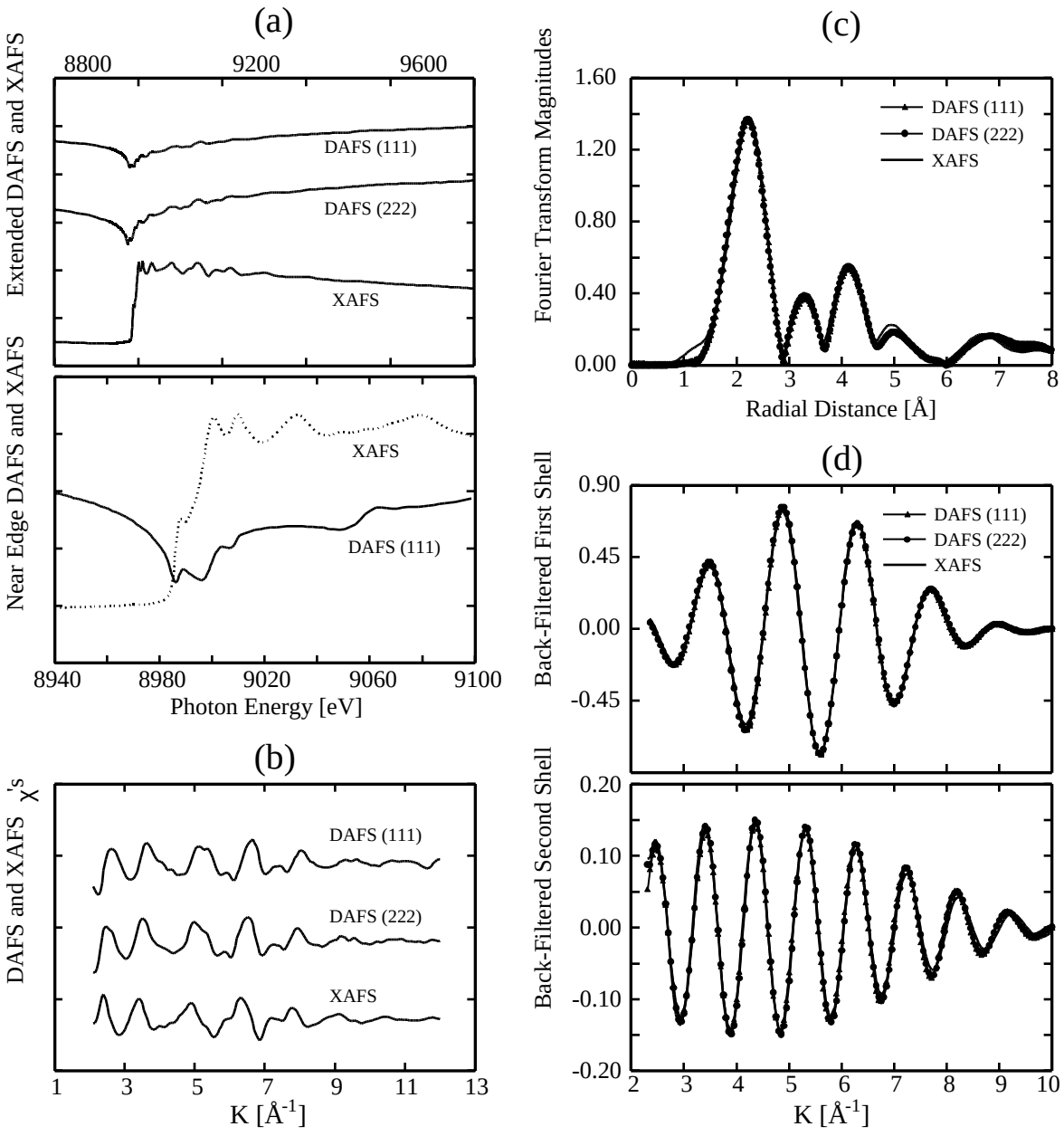

Figure 5. (a) The measured DAFS and XAFS intensities versus photon energy are shown in the extended region and in the near-edge region. (b) The background-subtracted and normalized DAFS and XAFS signals are shown versus photoelectron wavenumber, K. These three signals are each about 12% peak-to-peak of their corresponding cusp drop or edge step. (c) The Fourier transform magnitudes of the Cu(111) and Cu(222) DAFS and XAFS signals are shown versus the Fourier transform radial distance. (d) The Fourier back-filtered first and second shell DAFS and XAFS signals are shown for a single data set. The Cu(111) Bragg peak first and second shell DAFS signals have been shifted by 90°, demonstrating the $-\cos(2KR_j + \Phi_j)$ functional form of the Cu(111) DAFS χ_e signal, and the $\sin(2KR_j + \Phi_j)$ functional form of the Cu XAFS χ_μ signal. The Cu(222) first and second shell signals have been shifted by 67°, demonstrating the phase shift of the Cu(222) reflection due to the χ_μ and χ'' components.

within the experimental errors, each shell has the same phase shift for a fixed Bragg reflection. The apparent differences between the signals in Fig. 5b are caused by this phase shift of each shell.

The experimental DAFS-to-XAFS phase shifts determined from multiple back-filtered data sets, by assuming that the bond lengths for the XAFS signal were identical to those for the DAFS signal, are: Cu(111) first shell $90 \pm 6^\circ$ and second shell $83 \pm 12^\circ$; and Cu(222) first shell $70 \pm 6^\circ$ and second shell $64 \pm 12^\circ$. For the Cu(111) Bragg reflection, the χ'' DAFS contribution and the χ_μ absorption correction contribution accidently cancel, leaving only the $2(f_0 + f_s')f_s''\chi'$ oscillating DAFS contribution which has the form $-\cos(2KR_j + \Phi_j)$. Consequently, the Cu(111) first and second shells are simply shifted by 90° with respect to the Cu XAFS signal. For the Cu(222) Bragg reflection, the DAFS χ'' component is larger than the absorption χ_μ contribution. The measured phase shifts agree quite well with the values calculated using tabulated values of f_0, f_s', f_s'' and μ.

Without constraining the distances to be equal, and by using the XAFS ratio method [20] to calculate the relative bond length shift, ΔR, between each DAFS signal (treated as an "unknown") and the Cu XAFS signal (treated as a "known" standard), the following ΔR's are obtained: Cu(111) first shell 0 ± 0.005Å and second shell 0 ± 0.015Å; Cu(222) first shell 0 ± 0.015Å and second shell 0 ± 0.015Å. This demonstrates that DAFS measurements can be used to provide neighbor distances with accuracies comparable to XAFS measurements, and that experimental or theoretical XAFS standards can be used to analyze DAFS measurements by simply shifting the phases appropriately.

5.3. Kramers-Kronig analysis for Cu

The Kramers-Kronig transform analysis of the Cu DAFS and XAFS measurements was done in two different ways. First, the Kramers-Kronig transform of the normalized Cu(111) DAFS χ_e was compared to the XAFS χ_μ (see Fig. 6a); χ_e is dominated by χ' since the χ'' and χ_μ contributions accidentally cancel. The agreement is excellent. Second, the DAFS f' and f'' functions were extracted from the raw data using the Kramers-Kronig method. The resulting f' and f'' functions are compared in Fig. 6b with the Cromer-Liberman f_s' and f_s'' values.

The Kramers-Kronig method f' and f'' functions were splined to determine the associated DAFS χ' and χ'' functions. The resulting χ' and χ'' functions are compared with the normalized Cu(111) DAFS χ_e in Fig. 6c and with the XAFS χ_μ signals in Fig. 6d. The agreement between these signals is excellent. The Kramers-Kronig iterative fitting procedure is clearly a very useful method for analyzing DAFS data.

6. WAVEVECTOR SELECTIVITY

One important enhanced sensitivity of DAFS is its wavevector selectivity. Wavevector selectivity can be obtained whenever different spatial regions, or components, of the sample produce Bragg diffraction peaks at separable locations in reciprocal space. Then, the local atomic structure of each region can be determined by using one of its characteristic diffraction peaks, even when the different regions contain identical atomic types. Wavevector selectivity is not possible with XAFS measurements in general, be-

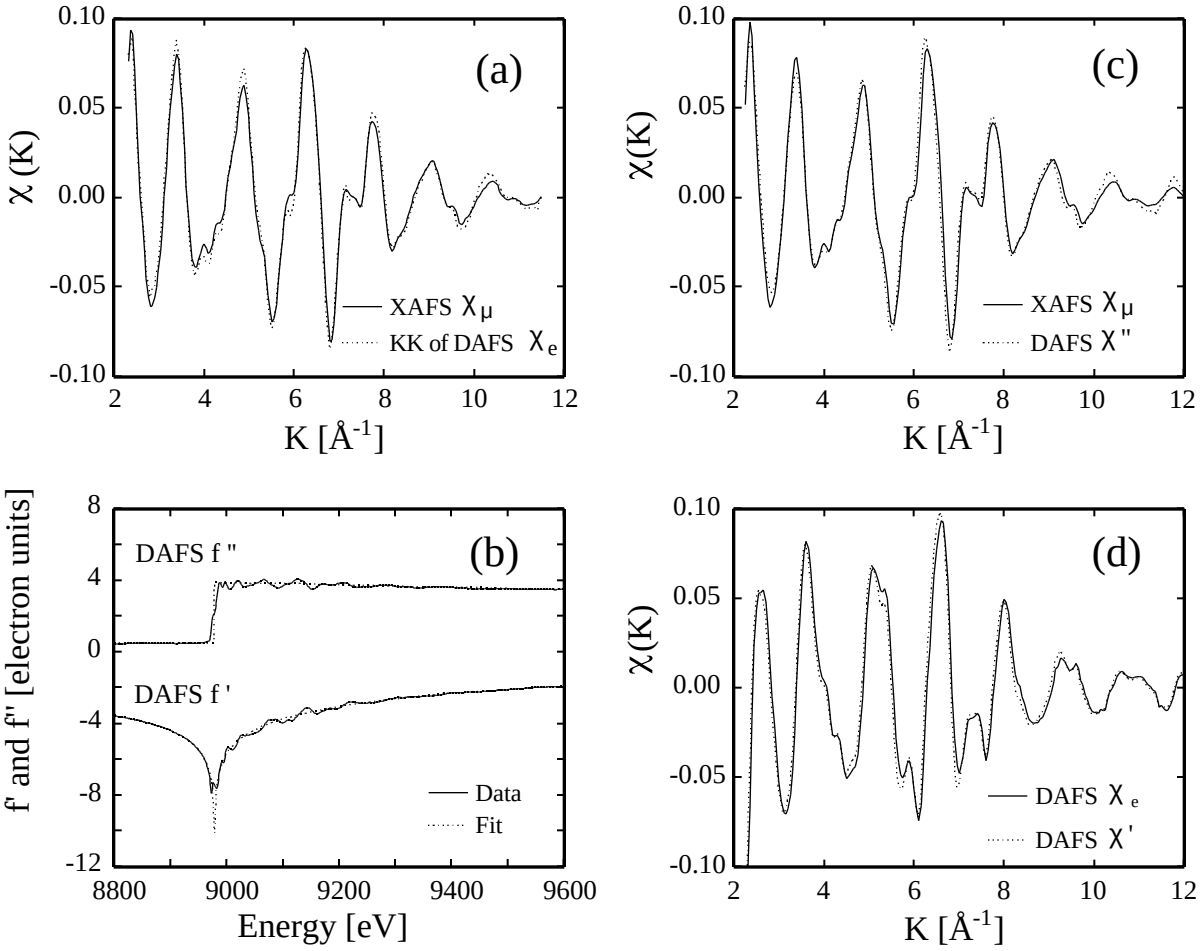

Figure 6. Demonstration of the Kramers-Kronig relationships between the DAFS χ' and χ'' signals and the XAFS χ_μ signal for Cu metal. (a) The agreement between the Kramers-Kronig transform of the Cu(111) DAFS χ_e and the normalized XAFS χ_μ. (b) Comparison of the Cromer-Liberman theoretical f_s' and f_s'' values and the measured DAFS f' and f'' values. (c) The agreement between the Kramers-Kronig method χ'' signal and the normalized XAFS χ_μ signal. (d) The agreement between the Kramers-Kronig method χ' signal and the normalized Cu(111) DAFS χ_e signal.

cause there is often no way to separate the absorption signals of the different regions or components. Some applications where the wavevector selectivity of DAFS can provide information that cannot be obtained using XAFS include: (1) strained and/or compositionally modulated layers, (2) mixed phase powders or composite materials, (3) buried layers, and (4) buried monolayers or reconstructed interfaces. The example described in this section is for a buried layer system. Examples of wavevector selective DAFS for mixed phase powders [9] and for buried monolayers [8, 25] have been reported by several groups.

6.1. DAFS measurements for InGaAs

A 400Å thick strained $In_{0.2}Ga_{0.8}As$ layer, grown epitaxially on GaAs, was chosen for this study. XAFS experiments could not be used to study the InGaAs local structure in this sample because of strong interfering signals from the GaAs substrate and cap. The structure of the GaAs/InGaAs/GaAs sample is shown in Fig. 7a. The lattice spacing of the 400Å InGaAs layer was larger than the lattice spacing of the GaAs substrate and cap, and the InGaAs diffraction peak was well separated from the GaAs peak. Figure 7b shows the measured x-ray diffraction pattern as a function of the Bragg angle 2θ near the GaAs (004) Bragg peak for a photon energy of E = 8047 eV. The intense peak at $2\theta \approx 66^\circ$ was produced by the GaAs substrate, while the broad peak at $2\theta \approx 64^\circ$ was produced by the InGaAs layer. The InGaAs peak is broad and has "subsidiary" side lobes, due to the finite thickness of the InGaAs layer. Because the InGaAs and GaAs peaks were well separated in 2θ, the Ga and As DAFS signals from the InGaAs peak could be measured without interference from the Ga and As in the substrate.

6.2. The virtual crystal model and the local structural model for InGaAs

To interpret the DAFS measurements, we used two standard models of the InGaAs crystal structure [26]. In the virtual crystal model (VCM), the atoms are located without local distortions at the "ideal" lattice sites of the average unit cell. The atoms remain on these ideal sites as the average unit cell expands or contracts. In the local structure model (LSM), the structure distorts locally to accomodate the average lattice constant changes, but keeps the near-neighbor distances roughly constant. This model attempts to keep the bond lengths fixed because it is much cheaper energetically to bend the bonds than it is to stretch them [27]. Our FEFF analysis described below shows that only the local structure model is consistent with the DAFS measurements.

Note that for simple tetragonal distortions, DAFS provides essentially a complete structural determination without a full crystallographic analysis since its diffraction signals provide the average layer spacings and its fine structure signals provide the average bond lengths. Analogous *separate* x-ray diffraction and XAFS measurements were shown previously to determine the detailed unit cell structure of tetragonally distorted strained layer GeSi samples [27].

6.3. FEFF analysis for InGaAs

For the As K-edge data, the results of the fits for the two models are compared in Fig. 7c. Note that the LSM fits both the first and second shells, but the VCM does not fit the first shell data, centered near $R = 2.1$Å, and also has errors for the second shell, centered near $R = 3.7$Å. The differences between the VCM and LSM fits for the first shell data are caused primarily by the different values of the two models for the As-In near-neighbor distance. To match the unit cell size, the VCM must have a shorter distance, 2.47Å, than the LSM distance, 2.60Å, which matches the bond length. In addition, the shorter LSM near-neighbor As-Ga distance, 2.45Å, compared with the 2.47Å VCM distance improves the fit. The bimodal As-As distribution used by the LSM improves the fit in the second shell region.

For the Ga K-edge data, the results of the fits for the two models are compared in Fig. 7d. Just as for the As K-edge data, the VCM does not fit the first shell data. This is primarily due to the long Ga-As near-neighbor distance for the VCM, 2.472Å, instead

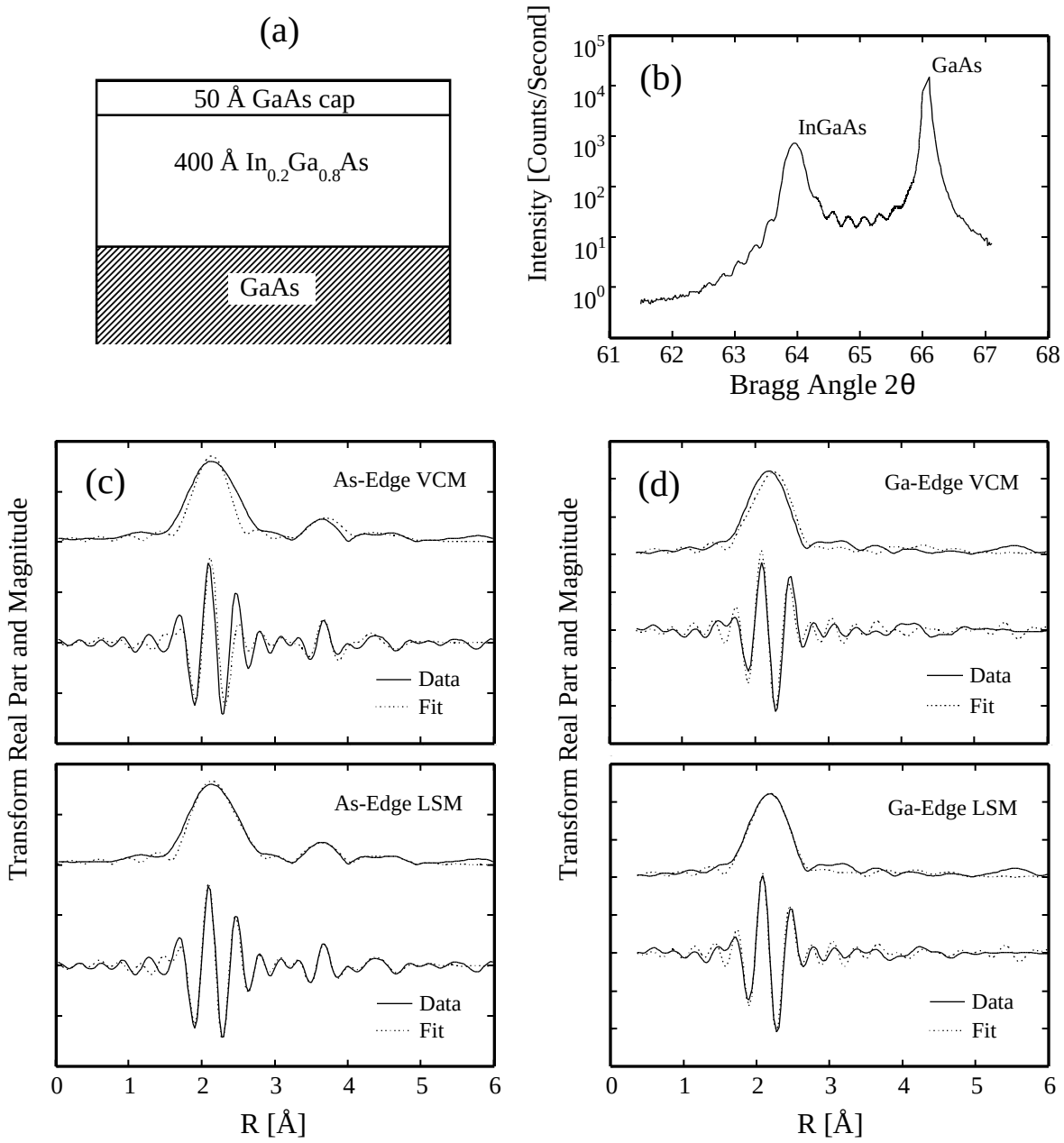

Figure 7. Demonstration of the wavevector selectivity of DAFS. (a) The multilayer GaAs/InGaAs/GaAs sample was a 400Å thick $In_{0.2}Ga_{0.8}As$ layer grown by MBE on a (001) GaAs substrate and capped with 50Å of GaAs. (b) The measured intensity versus the Bragg angle for the (004) reflections. Comparison of the virtual crystal model (VCM) fits and the local structure model (LSM) fits for: (c) the As K-edge data, and (d) the Ga K-edge data. Note that only the local structure model is consistent with the data; the virtual crystal model does not fit. These measurements show that the Ga-As, As-In, and As-Ga bond lengths in the InGaAs layer are very close to their corresponding undistorted values in GaAs and InAs.

of the LSM distance of 2.448Å. This difference is only 0.024Å, which indicates the sensitivity of DAFS (or XAFS) to the near-neighbor distances. Note that although neither model appears to fit the second shell data, the large Ga-Ga disorder actually precludes fitting this region—the apparent "signal" in this region is actually just truncation ripple from the first shell.

These results demonstrate that wavevector selective DAFS can be used to obtain precise local atomic structural information for specifically selected layers in both semiconductor and general multilayer samples, even in the presence of adjacent layers with the same atomic species.

7. SITE SELECTIVITY

Another important enhancement provided by DAFS is its site selectivity. Site selective DAFS measurements of crystallographically inequivalent Bragg reflections can be used to determine the XAFS-like information about the inequivalent sites within the unit cell even when these sites have the same atomic species. Because the DAFS intensity contains linear combinations of the contributions from the individual inequivalent sites, the specific site information can be obtained by resolving the individual contributions. In very favorable cases, some reflections will be dominated by a single site and the separation is easy [9]. In general, the individual contributions are not known and crystallographic procedures are needed. The $YBa_2Cu_3O_{7-\delta}$ superconductor is an attractive system to demonstrate site selectivity because the two inequivalent Cu sites play important roles in the material's superconductivity, and because there have been numerous previous XAFS studies of this system which can be compared with the DAFS results.

7.1. DAFS measurements for $YBa_2Cu_3O_{6.6}$

The sample was a 1 cm square 2400Å thick $YBa_2Cu_3O_{6.6}$ (001) film grown epitaxially on a MgO (001) substrate by pulsed laser deposition. The crystal was fully twinned in the ab plane and the c-axis mosaic spread was about 0.25° FWHM. The x-ray polarization was perpendicular to both the scattering plane and the c-axis of the crystal. Simultaneous fluorescence measurements were used for the absorption correction and were also used as an E_0 reference to facilitate accurate comparisons between different Bragg peaks. The DAFS signals were measured across the Cu K-edge for the eight different $(00L)$ Bragg peaks listed in Table 1. As illustrated in Fig. 8, the measured contrast is very different for different Bragg peaks. When the peak is weak, the oscillating DAFS terms, $2\,\mathrm{Re}(A_0)f_s''\chi'$ and $2\,\mathrm{Im}(A_0)f_s''\chi''$, are more important. The contrast is then larger and the DAFS signal can be measured more easily for these weak, high contrast reflections than it can for the strong, low contrast reflections, or for the XAFS. This contrast enhancement is not possible in conventional XAFS because the XAFS contrast is fixed by the relative numbers of inequivalent absorbing atoms (with the same atomic type). The DAFS intensities were corrected for absorption using the measured fluorescence XAFS χ_μ signal. The measured $\exp(-\mu x)$ values were converted to absorption coefficient values by fitting the measured XAFS to the smooth absorption coefficient calculated using the values of McMaster [28]. The properly normalized flu-

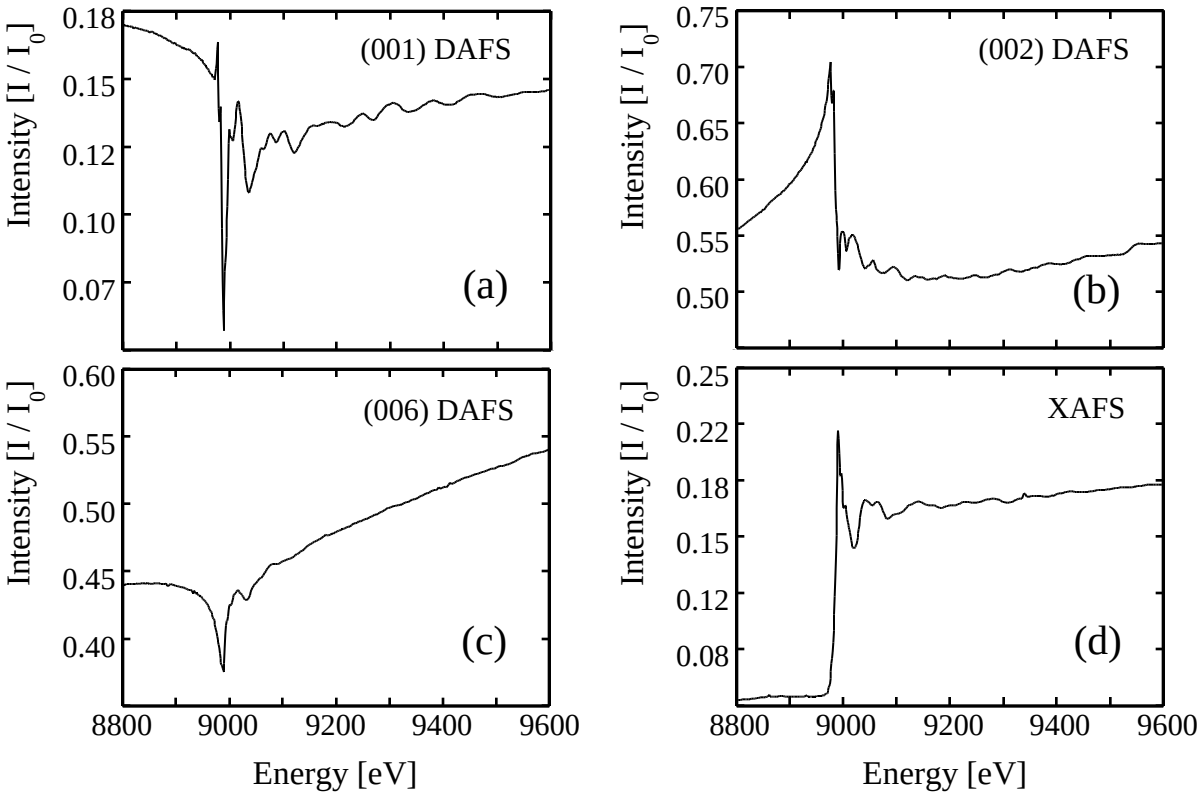

Figure 8. DAFS signals for a 2400Å thick film of $YBa_2Cu_3O_{6.6}$ grown epitaxially on a (001) MgO substrate. The (001), (002) and (006) Bragg reflections are shown in (a), (b) and (c) respectively. The fluorescence XAFS signal is shown in (d). Note the increased contrast for the weak (001) and (002) DAFS signals relative to the strong (006) DAFS and to the XAFS signals. The DAFS fine structure is larger for these weak Bragg reflections because the relative contributions from the resonant Cu atoms are larger.

orescence XAFS data was then used to construct the absorption correction function, $A(\mathbf{Q}, E)$. The measured DAFS data was also corrected for instrument contributions.

7.2. Separation of the two Cu sites in $YBa_2Cu_3O_{6.6}$

Site selectivity is produced by the variable Cu(1) and Cu(2) site contributions for different Bragg reflections. Table 1 lists the calculated values of the crystallographic weights for each site, α_1 and α_2, for the eight different $(00L)$ Bragg reflections that were measured. The weights were calculated using the atomic coordinates reported by Cava, *et al.* [29]. Note that there is considerable variation in the crystallographic weights for these eight $(00L)$ Bragg reflections. All of these reflections were easily accessible with the 2-circle spectrometer and the (001) film orientation. Also note that the calculated contributions of the two sites do not depend on the lattice constant, but only on the relative positions of the sites within the unit cell.

The Cu weights for the different Bragg reflections listed in Table 1 have two pri-

mary features. First, both sites contribute to all the Bragg reflections. Since a single Bragg reflection cannot be used to determine the local structure of a single Cu site, the contributions to several Bragg reflections are needed to resolve the individual sites. Second, the sign of the Cu(2) weight relative to the Cu(1) weight changes for different Bragg reflections. These sign changes increase the site separation sensitivity, and make it easy to assign near-edge features to a particular site. The assignment of the near-edge features based on these sign changes is discussed in Section 8.1.

7.3. Kramers-Kronig and FEFF analysis for $YBa_2Cu_3O_{6.6}$

The DAFS f' and f'' functions were isolated using the Kramers-Kronig method and the resulting f' and f'' functions were splined to obtain the corresponding χ' and χ'' functions. Because the χ' and χ'' functions contain linear combinations of contributions from the Cu(1) and Cu(2) sites, simple weighted differences between pairs of reflections could be used to obtain the site-separated contributions. The site-separated Cu(1) and Cu(2) Fourier transform magnitudes obtained by calculating weighted differences of the pairs using the crystallographic weights in Table 1, and then averaging over the pairs, are shown in Fig. 9. A FEFF calculation of the Fourier transform magnitudes expected for the *separate* Cu(1) and Cu(2) sites using the known $YBa_2Cu_3O_{6.6}$ structure are also shown. The agreement is very good and could probably be improved by allowing the crystallographic weights to vary slightly. These results clearly demonstrate the potential of EDAFS for site-selective short-range atomic structural studies.

8. DANES STUDY OF $YBa_2Cu_3O_{6.6}$

The x-ray absorption fine structure in the near-edge region is called the x-ray absorption near-edge structure (XANES), and, by analogy, the same structure in the elastic

Table 1
The crystallographic weights and fitting parameters for eight $YBa_2Cu_3O_{6.6}$ Bragg reflections. By choosing the origin of the coordinate system at a Cu(1) site, we have set the crystallographic weight for the Cu(1) site, $\alpha_1 = 1$. The crystallographic weight for the Cu(2) sites is then given by $\alpha_2 = 2\cos(\mathbf{Q} \cdot \mathbf{r}_2)$. The values of β and γ calculated using the structure reported by Cava *et al.* and derived from the Kramers-Kronig fits, and the measured Bragg intensities relative to the (006) reflection at $E = 8800$ eV are also shown.

Peak	α_1	α_2	β_c	γ_c	β_f	γ_f	I/I(006)
001	1.00	-1.23	0.0368	-0.630	0.0403	-0.500	0.135
002	1.00	-0.50	-0.0268	0.405	-0.0348	0.668	0.189
003	1.00	1.84	-0.0608	0.310	-0.0770	0.480	0.463
004	1.00	-1.75	0.0363	-0.014	0.0376	0.017	0.042
005	1.00	0.31	0.0132	0.105	0.0145	-0.010	0.636
006	1.00	1.37	0.0158	0.083	0.0156	0.041	1.000
007	1.00	-1.99	0.0163	0.079	0.0183	0.075	0.116
009	1.00	0.68	-0.0353	0.195	-0.0400	0.282	0.039

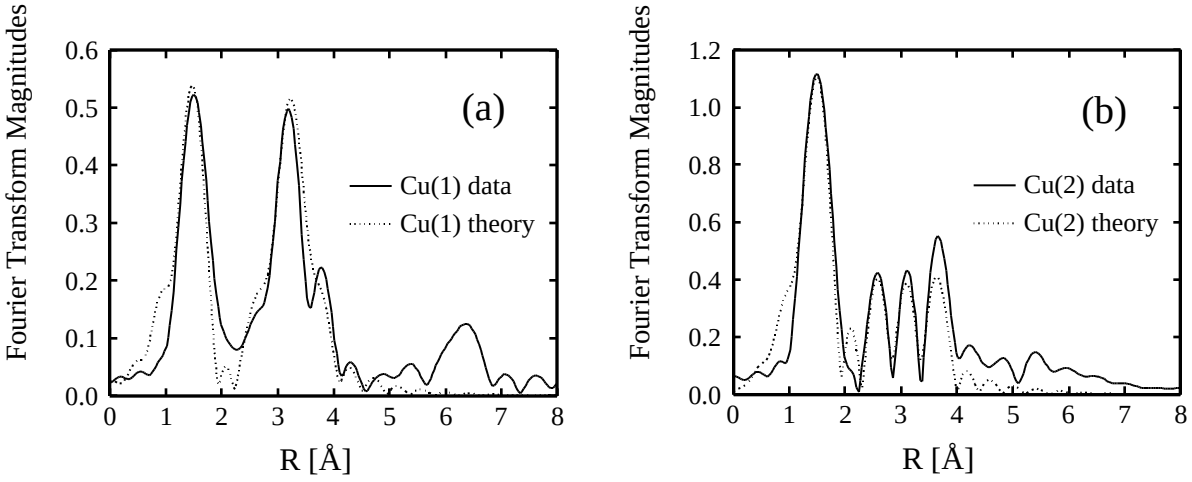

Figure 9. Demonstration of the site selectivity of DAFS. The site separated Cu(1) and Cu(2) Fourier transform magnitudes are compared with the predictions of FEFF. The agreement is very good and can probably be improved by allowing the atomic positions to vary slightly from their literature values [29].

scattering channel is called the diffraction anomalous near-edge structure (DANES). Just as EDAFS combines diffraction and EXAFS, DANES combines the wavevector and site selectivity of diffraction with the valence, empty orbital, and structural sensitivity of XANES. Consequently, for crystals with inequivalent sites, DANES can assign near-edge features to specific sites. However, in this region (i.e., within about 30 eV of the edge energy) the low energy photoelectrons are very strongly scattered by the surrounding atoms, producing large multiple scattering effects, and making the data analysis considerably more demanding than it is in the extended fine structure region. The recent advances in MS-XAFS and MS-DAFS theory and analysis now allow the full curved-wave multiple-scattering effects to be calculated almost down to the continuum threshold [4]. There are also separate codes for calculating the DANES and XANES signals which involve transitions to the bound states below the continuum threshold [30]. DANES and XANES will become much more useful, however, when convenient analysis methods that allow accurate predictions of the near-edge structure, including both the multiple-scattering and bound state effects, are developed.

An example of the ability of DANES to assign features in the near-edge region to specific sites is provided by the application of DANES techniques to separate the near-edge signals for the two inequivalent Cu sites in the $YBa_2Cu_3O_{6.6}$ superconductor film described in the previous section. In the case of $YBa_2Cu_3O_{7-\delta}$, the original assignment of near-edge features to particular Cu sites was difficult and controversial [31]. While site specific assignments were eventually made using polarized XANES measurements on oriented grains [32], and on single crystals [33], the site selectivity of the DANES measurements presented here provide much cleaner and much easier assignments.

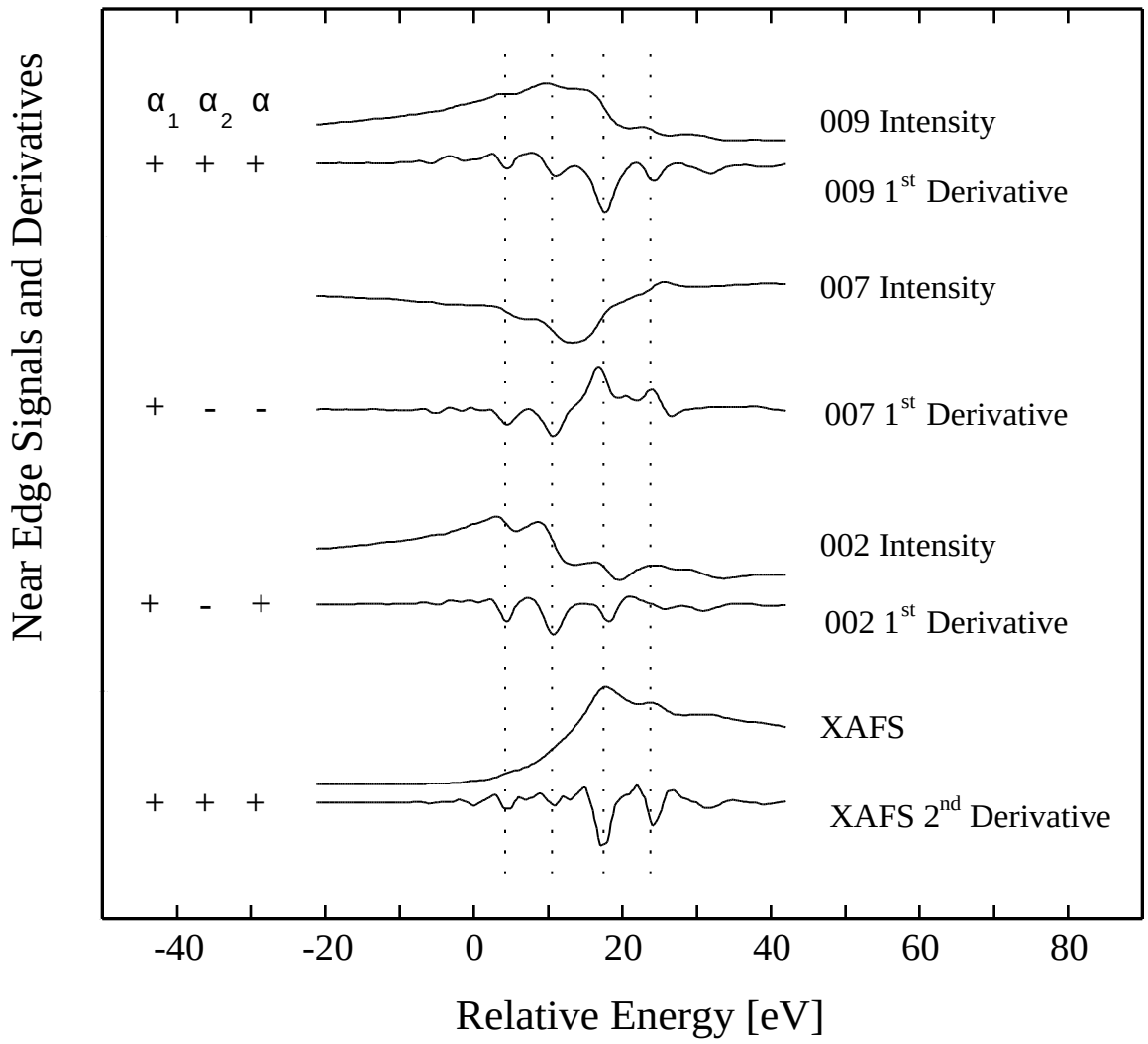

Figure 10. Comparison of the site-sensitive DANES signals and the (effectively site averaged) XANES signal for the $YBa_2Cu_3O_{6.6}$ superconductor film. The measured (009), (007), and (002) DANES intensities and the fluorescence XANES intensity are shown versus photon energy measured relative to the Cu metal edge energy. The first derivatives of the DANES intensities, with respect to energy, and the second derivative of the XANES intensity, with respect to energy, are also shown. The signs of the Cu(1) and Cu(2) contributions, α_1 and α_2, and of the net Cu(1) and Cu(2) contribution, $\alpha = \alpha_1 + \alpha_2$, are shown beside each derivative. Four characteristic features in the DANES and XANES derivatives are indicated by the dotted lines. Note that the first two (lower energy) features have minima that correlate with the sign of the Cu(1) contribution, indicating that these features are primarily associated with the Cu(1) site. Similarly, the second two (higher energy) transitions have maxima or minima that correlate with the sign of the net contribution, indicating that they are associated with both sites. These signals demonstrate the utility of DANES for assigning site-specific features in the valence sensitive near-edge region.

8.1. Rapid site assignments of $YBa_2Cu_3O_{6.6}$ XANES features using DANES

The ease with which DANES can be used to assign near-edge features to specific inequivalent sites in $YBa_2Cu_3O_{6.6}$ is illustrated in Fig. 10, which compares the DANES signal from three Bragg reflections with the XANES signal. The energy positions of previously identified transitions [31] in the near-edge region were assigned using the extrema of the second energy derivatives of the XANES signal. Since the Kramers-Kronig relation between absorption and scattering is similar to a derivative, the same near-edge features appear as first energy derivatives of the DANES signal. Consequently, Fig. 10 shows the first derivatives of the DANES signals and the second derivative of the XANES signal. Note that the two transitions at 4.6 and 10.8 eV have minima that correlate with the sign of the Cu(1) site contribution, indicating these two features are dominated by Cu(1) site contributions. The two features at 17.0 and 24.0 eV have maxima or minima that correlate with the sign of the net Cu contribution, *i.e.*, with the sign of α, and therefore have contributions from both sites. These DANES assignments are consistent with the assignments based on polarized XANES, but are extremely simple compared to the XANES work since the sign of the first energy derivative of the DANES signals is sufficient to make the assignments.

8.2. Kramers-Kronig analysis of the $YBa_2Cu_3O_{6.6}$ signals

Because the DANES signals contain linear combinations of contributions from the two Cu sites, the individual site contributions can be resolved. The site-separated f' and f'' functions for the two copper sites are shown in Fig. 11. These site separated signals were obtained by calculating crystallographically weighted differences of six pairs of Kramers-Kronig method f' and f'' functions. The near-edge feature assignments made using the signs of the first energy derivatives shown in Fig. 10 are confirmed by the detailed analysis shown in Fig. 11. The detailed analysis also shows that there are energy shifts between the two sites, *e.g.,* 0.9 ± 0.3 eV for the transition near 17.0 eV.

8.3. Polarized XANES and DANES measurements

An important aspect of high-T_c superconductor research is the connection between the hole concentration in the Cu x^2-y^2 bands, the Cu valence, and the T_c of the material. In the $YBa_2Cu_3O_{7-\delta}$ high-T_c superconductors, the Cu(2) bond valence sum has been shown [29] to have the same shape versus δ as T_c, while the bond valence sum of the Cu(1) chain atoms has a linear dependence on oxygen content and is independent of the material's superconductivity. Polarized XANES measurements have been very useful in studies of new high-T_c materials. For example, the $3d$ valence electronic configuration of the Cu atoms in $YBa_2Cu_3O_{7-\delta}$ was determined by comparing the XANES features of $YBa_2Cu_3O_{7-\delta}$ to XANES fingerprints of closely related Cu-O compounds [32]. Since DANES methods provide precise, and very easy, assignments of near-edge features to specific sites, DANES studies should prove useful in site-specific valence determinations of high-T_c and other materials. In addition, because the tensor properties of the DANES signals are sensitive to the empty orbital symmetries and occupations, there is considerable interest in applying tensor DANES to make site-specific empty orbital maps [34].

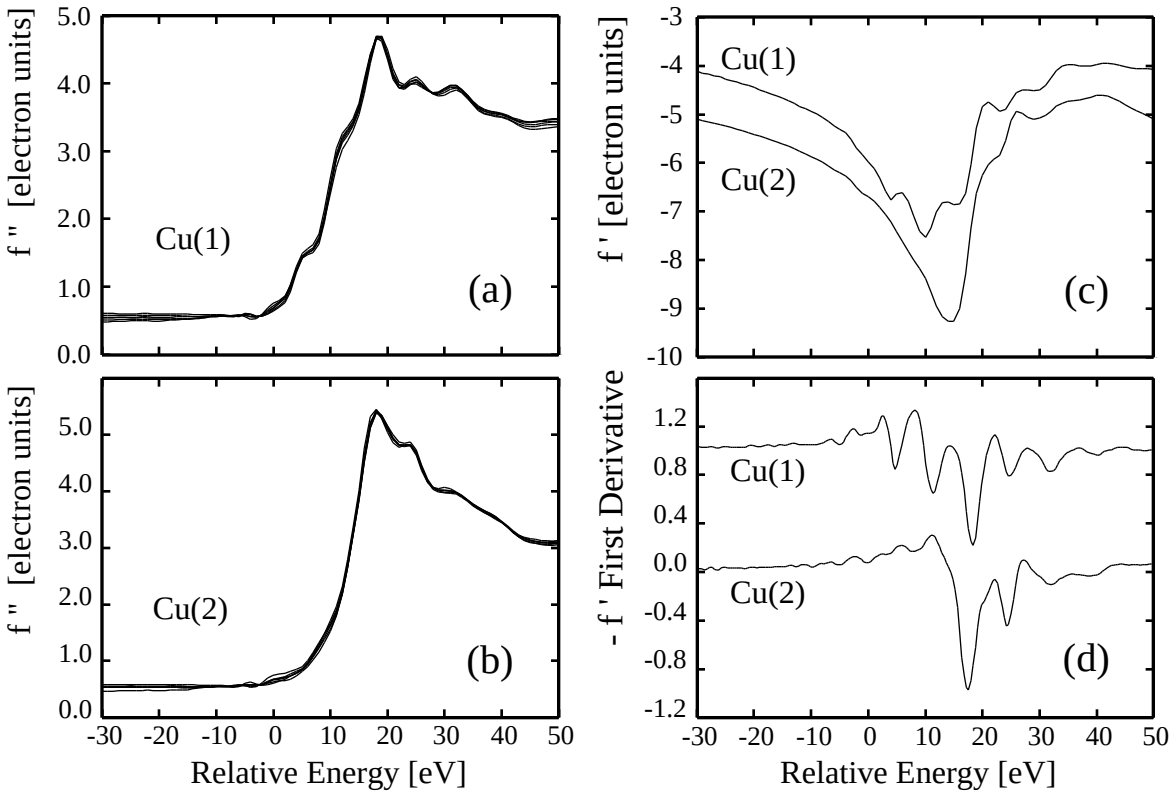

Figure 11. The site-separated DANES functions, f' and f'', for $YBa_2Cu_3O_{6.6}$. (a) f'' for the Cu(1) site. (b) f'' for the Cu(2) site. Parts a and b are overplots of the f'' functions obtained for six different pairs of Bragg reflections and illustrate the precision of the data and of the analysis. (c) The average f' functions for the Cu(1) site and for the Cu(2) site calculated by averaging the f' signals for the same six pairs of reflections shown in parts a and b. (d) The negative energy derivatives, $-df'/dE$, of the f' functions shown in part c. For clarity, the Cu(1) site signals in parts c and d are shown displaced vertically by +1.00 above the Cu(2) site signals.

9. DISCUSSION

In the previous sections of this chapter, we have described the current state of the rapidly developing DAFS technique. This section contains our ideas and speculations about the near-future evolution of DAFS. Many of these anticipated developments depend on third-generation synchrotron sources.

9.1. Powder DAFS

There have already been demonstration experiments showing that the wavevector and site selectivities of DAFS can be obtained using synchrotron powder diffraction [9]. There has also been considerable powder diffraction community interest in the valence and orbital sensitivity provided by the DANES features [35]. It has been difficult, however, to obtain adequate diffracted beam intensities using second-generation

synchrotron radiation sources equipped with conventional detectors. In addition, the absorption corrections and background fluorescence problems are much more severe for powder samples than they are for the thin epitaxial film samples described in this chapter. The availability of third-generation synchrotron radiation sources and of better detectors will enhance the capabilities of powder DAFS. Detectors which provide energy discrimination (to remove the fluorescence) and which provide parallel data acquisition over the full Debye-Sherrer ring or at many simultaneous 2θ values (to provide more signal) will allow greatly improved measurements at second- or third-generation sources.

9.2. Magnetic DAFS

There have been beautiful recent developments in the use of magnetic circular x-ray dichroism (MCXD) to study magnetic materials [36–38]. MCXD measurements provide element-specific information about the magnetic environment of an absorbing atom from the difference in the x-ray absorption coefficient for right and left circularly polarized x rays. In just the same way that DAFS is the diffraction analog of XAFS, and provides site-specific local structural information, McDAFSis the diffraction analog of MCXD (*viz.*, McXAFS), and provides site-specific local magnetic information. McXANES and McDANES probe the empty density of magnetic states near threshold. McEXAFS and McEDAFS probe the radial distribution of the magnetization of the atoms surrounding the excited atom [37]. MCXD microscopy has been done [38] with a resolution of about 1 micron by imaging the emitted photoelectrons. McDAFS studies can be done with comparable, or even smaller, spatial resolution using x-ray capillary optics [39]. The first site-separated McDANES results have recently been reported [40].

The primary motivation for doing McDAFS instead of MCXD is to obtain the site-selectivity produced by the crystallographic sensitivities of DAFS. This will allow element-specific and site-specific determinations of the density of magnetic states near threshold (from the McDANES) and of the radial distribution of the magnetic neighbors surrounding the excited atom (from the McEDAFS). McDAFS provides the only way to directly measure the complete, detailed, site-separated, local magnetic environment and properties of specific elements at specific sites. The wavevector selectivity of McDAFS should also prove useful in studies of magnetic multilayers since it will allow the signals from the same element type in the different layers to be separated.

9.3. Polarization analyzed DAFS

The electric dipole components usually dominate the DAFS transitions, and consequently the polarization selection rules are usually pure electric dipole rules. For linearly polarized incoming radiation and a pure electric dipole transition (*i.e.*, no magnetic effects, chirality or dichroism), the outgoing radiation will have the same linear polarization as the incoming radiation. If there is a small additional component of electric quadrupole scattering, it can be measured easily and accurately by using a crossed polarizer to remove the electric dipole component.

A complete DANES polarization analysis versus photon energy will allow the symmetry and density of the empty antibonding and low continuum states to be determined. If the material is dichroic, chiral and/or magnetic, these additional effects can also be distinguished via a complete polarization analysis. DAFS polarization analysis represents an infusion of spectroscopic methods into crystallography, and vice versa; this will

have important consequences for both fields. For example, the usual forbidden reflection rules of crystallography are based on electric dipole transitions, and it has been shown that these rules are modified in useful ways for resonantly excited transitions [14, 34, 41].

9.4. Crystallographic DAFS studies

The use of the tensor DANES features to enhance conventional scalar crystallography are discussed by Templeton, Blume, Kirfel, Finkelstein, and Morgenroth *et al* in this book. Such x-ray "tensor crystallography" using near-edge features is now being widely developed.

The scalar and tensor DAFS information in the extended region can also be incorporated into crystallography. The co-refinement of the diffraction-like and EXAFS-like sensitivities of EDAFS is described below.

9.4.1. Co-refinement of the EDAFS information

One of the interesting questions about the structure of alloys and of substitutionally doped materials is the nature of the disorder produced by the alloying or by the substitutional doping. Previously, the long-range order sensitivity of diffraction and the short-range order sensitivity of EXAFS *measured separately* have been used to provide complementary views of the true structure as a long-range ordered "virtual crystal" modulated by short-range distortions. For example, separate diffraction and XAFS results have been combined to probe the local distortions in the structure of strained pseudomorphic GeSi layers [27] and of binary salts [42]. These studies showed that the actual structures are distorted versions of the original lattices. EDAFS measurements enhance this capability, since measurements can be made on the same samples, at the same time, under the same conditions. Thus, the long- and short-range order information is guaranteed to be consistent.

It will be very interesting to do "EDAFS crystallography" by co-refining the atomic positions using all of the Bragg peak intensities, measured over a continuous range of energies, at the same time. This will force the atomic positions to simultaneously fit EDAFS's long-range diffraction information and short-range fine structure information. This combination of long-range and short-range information is reminiscent of the use of the short-range sequence information in protein crystallography. It will also be very interesting to apply EDAFS co-refinement techniques to structural phase transitions which involve order-disorder contributions to the transition.

Note that EDAFS crystallography also incorporates simultaneously both the diffraction Debye-Waller factors (reflecting the anisotropic mean-square atomic displacements from the equilibrium atomic positions) *and* the XAFS-like Debye-Waller factors (reflecting the mean-square multi-leg path length variations from the equilibrium path lengths). Thus specific correlated motions can be determined from the EDAFS co-refinement.

9.5. DAFS on non-crystalline materials

The crystallographic and diffraction sensitivities of DAFS that enhance XAFS come from the Fourier transform nature of diffraction. This allows DAFS to pick out specific Fourier components of the density. How much of this crystallographic utility persists when DAFS is applied to less-ordered materials? Some of the interesting systems are

quasicrystals, amorphous materials and liquids. Even in these systems the diffraction condition still selects a specific wavevector component of the density. So, roughly speaking, DAFS will provide the XAFS-like radial distribution function of the atoms surrounding the resonantly selected element type, weighted by the contribution of the resonantly scattering atom to the specific Fourier component of the density selected by the diffraction condition.

Standard crystallography cannot fully solve the structure of quasicrystals because the necessary diffraction information is distributed throughout reciprocal space in infinitely many weak "quasi-Bragg" peaks. This provides the motivation for pursuing further structural information with DAFS. Will all of the strong quasi-Bragg DAFS intensities look the same, or will they look different? The same question arises in amorphous materials and liquids: Does the EDAFS radial distribution function depend on the diffraction wavevector? It is known that the differential anomalous scattering (DAS) does depend on the diffraction wavevector for compositionally modulated glasses [43]. In this case, the different atom types appear preferentially at specific diffraction wavevectors, and consequently the DAS signals vary with the diffraction momentum transfer. What new structural and spectroscopic information can be obtained from EDAFS and DANES studies of non-crystalline materials?

The formal reason that DAFS can be used, in principle, to obtain more information about disordered and non-crystalline materials than conventional anomalous scattering, is that DAFS is sensitive to the pair and multiparticle correlation functions, while conventional anomalous diffraction is only sensitive to the pair correlation functions. DAFS is sensitive both to the pair and to the multiparticle correlation functions for several reasons: (1) Some of the oscillatory fine structure is produced by the interference effects of multi-leg photoelectron paths which include many (3, 4, 5, ...) atoms; the analogous sensitivity of XANES spectra to higher order correlations has been studied for over ten years [44]. (2) DAFS selects one wavevector with its diffraction condition (which is sensitive to the pair correlation functions) and then probes the associated multiparticle correlation functions with its fine structure signals. (3) Polarization analyzed DAFS probes the initial and final legs of the photoelectron path with more sensitivity than polarization analyzed XAFS because both the incident and the scattered photon polarizations, $\hat{\mathbf{e}}_1$ and $\hat{\mathbf{e}}_2$, can be varied independently. There has been a recent theoretical discussion of the potential application of some of these sensitivities to studies of the ternary correlation functions of amorphous systems [45].

10. CONCLUSION

The DAFS technique is one of the rapidly developing structural, spectroscopic, and crystallographic methods that have been stimulated by the availability of spectacular new synchrotron radiation sources. The benefits of infusing crystallographic methods into x-ray absorption spectroscopy have been clearly demonstrated. The theory of DAFS away from the edge is well developed and in good agreement with experiment, but a practical near-edge theory is still needed. The reverse benefits that the x-ray spectroscopic sensitivities can bring to crystallography are also of great interest and are currently being developed, as illustrated throughout this book. This widespread

work on the smooth and oscillatory scalar and tensor scattering amplitudes of atoms in condensed matter has turned these "previous problems" into "new solutions".

Truly comprehensive techniques should use all of the degrees of freedom of the photons: their momenta, energies and spins. Polarization analyzed DAFS uses all of these degrees of freedom in the special case of elastic scattering—there is momentum transfer, but no energy transfer. The three other closely related possibilities: 1) elastic forward scattering—no energy or momentum transfer, 2) absorption and inelastic forward scattering—energy, but no momentum transfer, and 3) inelastic resonant scattering (x-ray Raman)—both energy and momentum transfer, are all discussed in this book.

However, this book also teaches us that to encompass all resonant x-ray scattering processes, the above classification must be further enlarged to include the photon spin-angular momentum transfer and the coupling of the photon simultaneously to the charge and to the magnetism of condensed matter systems. The prospects for exciting future developments in resonant x-ray scattering seem very bright!

REFERENCES

1 The first experimental reports of x-ray absorption fine structure were by H. Fricke, Phys. Rev. **16** (1920) 202 and by G. Hertz, Z. Phys. **3** (1920) 19.

2 The earliest experimental report of diffraction fine structure that we are aware of is by Y. Cauchois and C. Bonnelle, C.R. Acad. Sci. (Paris) **242** (1956) 100 and 1596.

3 In this chapter, we follow the current international standard notation for the x-ray absorption acronyms: thus XAFS (x-ray absorption fine structure) includes both the EXAFS (extended x-ray absorption fine structure) and the XANES (x-ray absorption near edge structure). We use diffraction acronyms which are homologous to the standard absorption acronyms: thus DAFS (diffraction anomalous fine structure) includes both the EDAFS (extended diffraction anomalous fine structure) and the DANES (diffraction anomalous near edge structure).

4 The recent advances in MS-XAFS theory and analysis are described in J.J. Rehr, Japanese J. Appl. Phys. **32** Suppl. 32-2 (1993) 8; S.I. Zabinsky, *Multiple Scattering Theory of XAFS*, Ph.D. Thesis, University of Washington (1993); J.J. Rehr, R.C. Albers, S.I. Zabinsky, Phys. Rev. Lett. **69** (1992) 3397; J.J. Rehr, J. Mustre de Leon, S.I. Zabinsky, and R.C. Albers, J. Amer. Chem. Soc. **113** (1991) 5135.

5 Previous experimental and theoretical diffraction fine structure work includes: Y. Heno, C.R. Acad. Sci. (Paris) **242** (1956) 1599; G. Wendin, Phys. Scr. **21** (1979) 535; T. Fukamachi, S. Hosoya, T. Kawamura and J. Hastings, J. Appl. Cryst. **10** (1977) 321; D.M. Barrus, R.L. Blake, A.J. Burek, K.C. Chambers, and L.E. Cox, Phys. Rev. B **22** (1980) 4022; S.I. Salem and V.L. Hall, J. Phys. F **10** (1980) 1627; D.H. Templeton, L.K. Templeton, D.C. Phillips and K.O. Hodson, Acta Cryst. A**36** (1980) 436; V. Ponomarev and Y.A. Turutin, Sov. Phys. Tech. Phys. **29** (1984) 232; I. Arčon, A. Kodre, D. Glavič and M. Hribar, J. Phys. (Paris) **C9** (1987) 1105; I. Arčon, A. Kodre and M. Hribar, in *Second European Conference on Progress in X-Ray Synchrotron Radiation Research*, edited by A. Balerna, E. Bernieri and S. Mobilia (Italian Physical Society, Bologna, 1990) p. 419; I. Arčon, A. Kodre and M. Hribar, in *X-Ray Absorption Fine Structure*, edited by S. S. Hasnain (Ellis Horwood,

London, 1991) p. 726.
6 H. Stragier, J.O. Cross, J.J. Rehr, L.B. Sorensen, C.E. Bouldin and J.C. Woicik, Phys. Rev. Lett. **69** (1992) 3064.
7 C.E. Bouldin, J.C. Woicik, H. Stragier, J.O. Cross, J.J. Rehr and L.B. Sorensen, Japanese J. Appl. Phys. **32** Suppl. 32-2 (1993) 198.
8 D.J. Tweet, K. Akimoto, I. Hirosawa, T. Tatsumi, H. Kimura, J. Mizuki, L.B. Sorensen, C.E. Bouldin and T. Matsushita, Japanese J. Appl. Phys. **32** Suppl. 32-2 (1993) 203.
9 I.J. Pickering, M. Sansone, J.J. Marsch and G.N. George, Japanese J. Appl. Phys. **32** Suppl. 32-2 (1993) 206 and J. Amer. Chem. Soc. **115** (1993) 6302.
10 D.C. Bazin and D.A. Sayers, Japanese J. Appl. Phys. **32** Suppl. 32-2 (1993) 249 and 252.
11 H.J. Stragier, *DAFS: A New X-Ray Structural Technique*, Ph.D. Thesis, University of Washington (1993).
12 *N.B.*, the most natural sign convention is f_0 negative, f' a positive cusp, and f'' a positive step. The almost universal convention is f_0 positive, f' a negative cusp, and f'' a positive step, and we follow this "visual" convention in all of our figures. Our equations, however, are in "natural" units. Also note that the amplitude produced by a wave scattered from a plane of atoms has an additional phase shift of $-i$; see, *e.g.*, B.L. Henke, E.M. Gullikson and J.C. Davis, Atom. Nucl. Data Tables **54** (1993) 181 and **55** (1993) 349.
13 John S. Toll, Phys. Rev. **104** (1956) 1760.
14 For a review of anomalous scattering and references, see D.H. Templeton in *Handbook on Synchrotron Radiation*, edited by G. Brown and D.E. Moncton (Elsevier, Amsterdam, 1991) p. 201.
15 See L. Davidovich and H.M. Nussenveig, in *Foundations of Radiation Theory and Quantum Electrodynamics* edited by A.O. Barut (Plenum, New York, 1980) p. 83.
16 See the articles by M. Blume, by R.H. Pratt, L. Kissel and P.M. Bergstrom, Jr., and by C.T. Chantler in this book, and references therein.
17 H.K. Wagenfeld, Z. Phys. B **65** (1987) 437, and references therein.
18 D.T. Cromer and D. Liberman, J. Chem. Phys. **53** (1970) 1891, and Acta Cryst. A **37** (1981) 267; S. Sasaki, *Numerical Tables of Anomalous Scattering Factors Calculated by the Cromer and Liberman Method* KEK Report **88-14** (1989), and references therein.
19 J.J. Rehr, C.H. Booth, F. Bridges and S.I. Zabinsky, "X-ray Absorption Fine Structure in Embedded Atoms", University of Washington preprint (1993), accepted for publication in Phys. Rev. B.
20 *X-ray Absorption: Principles, Applications, Techniques of EXAFS, SEXAFS and XANES*, edited by R. Prins and D. Koningsberger (Wiley, New York, 1988).
21 K.H. Kim, M.T. Bell, R.K. Freitag, C.M. Dozier and C.E. Bouldin, Rev. Sci. Inst. **62** (1991) 982.
22 F.W. Lytle, R.B. Gregor, D.R. Sandstrom, E.C. Marques, J. Wong, C.L. Spiro, G.P. Huffman and F.E. Huggins, Nucl. Inst. Meth. **226** (1984) 542.
23 For a detailed recent experimental application of FEFF analysis techniques to XAFS, see A.I. Frenkl, E.A. Stern, M. Qian and M. Newville, Phys. Rev. B **48**

(1993) 12449.
24 See E.A. Stern, Phys. Rev. B **48** (1993) 9825, and references therein.
25 See the article by F.J. Walker and E.D. Specht in this book, and references therein.
26 J.C. Mikkelsen, Jr. and J.B. Boyce, Phys. Rev. B **28** 7130 (1983).
27 J.C. Woicik, C.E. Bouldin, M.I. Bell, J.O. Cross, D.J. Tweet, B.D. Swanson, T.M. Zhang, L.B. Sorensen, C.A. King, J.L. Hoyt, P. Pianetta, and J.F. Gibbons, Phys. Rev. B **43** (1991) 2419.
28 W.H. McMaster, N.K. DelGrande, J.H. Mallett and J.H. Hubbel, *Compilation of X-ray Cross Sections*, Lawrence Radiation Laboratory, Report UCRL-50174 (1969).
29 R.J. Cava, A.W. Hewat, E.A. Hewat, B. Batlogg, M. Marezio, K.M. Rabe, J.J. Krajewski, W.F. Peck Jr., and L.W. Rupp Jr., Physica C **165** (1990) 419.
30 For a current review of XANES theoretical and experimental methods and references, see J. Stöhr, *NEXAFS Spectroscopy*, (Springer-Verlag, Berlin, 1992).
31 J. Röhler, A. Larisch and R. Schafer, Physica C **191** (1992) 57.
32 See, for example, S.M. Heald, J.M. Tranquada, A.R. Moodenbaugh, and Youwen Xu, Phys. Rev. B **38** (1988) 761.
33 See, for example, H. Tolentino, E. Dartyge, A. Fontaine, G. Tourillon, T. Gourieux, G. Krill, M. Marer, and M.-F. Ravet, in *High-T_c Superconductors: Electronic Structure*, edited by A. Bianconi and A. Marcelli (Pergamon, Oxford, 1989) p. 245.
34 See the article by K.D. Finkelstein, M. Hamrick and Q. Shen in this book.
35 For current reviews of powder diffraction using synchrotron radiation and references, see the articles by D.E. Cox and A.P. Wilkinson and by W. Limper and W. Prandl in this book.
36 See the article by G. Schütz in this book, and also: G. Schütz, Physica Scripta T **29** (1989) 712; G. Schütz, P. Fischer, S. Stähler, M. Knülle and K. Attenkoffer, Japanese Journal of Applied Physics **32** Suppl. 32-2 (1993) 869.
37 G. Schütz, R. Wienke, W. Wilhelm, P. Kienle, R. Zeller, R. Frahm and G. Materlik, Phy. Rev. Lett. **58** (1987) 737.
38 J. Stöhr, Y. Wu, B.D. Hermsmeier, M.G. Samant, G.R. Harp, S. Koranda, D. Dunjam, B.P. Tonner, Science **259** (1993) 658.
39 D.H. Bilderback, S. A. Hoffman and D. J. Thiel, Science **263** (1994) 201.
40 H. Kawata, Abstract MS-01.04.05, XVI Congress and General Assembly of the International Union of Crystallography, Beijing (1993), and private communication.
41 See the articles by D. H. Templeton, by A. Kirfel, and by W. Morgenroth, A. Kirfel and K. Fischer in this book.
42 A. Frenkel, E.A. Stern, A. Voronel, M. Qian and M. Newville, Phys. Rev. Lett. **71** (1993) 3485.
43 P.H. Fuoss, P. Eisenberger, W.K. Warburton and A. Bienenstock, Phys. Rev. Lett. **46** (1981) 1537, and J.B. Kortright, W.K. Warburton, and A. Bienenstock, in *EXAFS and Near Edge Structure* edited by A. Bianconi, L. Incoccia and S. Stipcich (Springer-Verlag, Berlin, 1983) p. 362.
44 For a recent survey and references, see A. Filipponi and A. DiCicco, Sync. Rad. News **6**, No. 1 (1993) 13.
45 R.V. Vedrinskii, V.L. Kraizman, A.A. Novakovich and V.S. Machavariani, J. Phys. Condens. Matter **4** (1992) 6155.